PHOTON: SPEEDUP VOLUME UNDERSTANDING WITH EFFICIENT MULTIMODAL LARGE LANGUAGE MODELS

Chengyu Fang[1,2,*] **Heng Guo**[2,3,*] **Zheng Jiang**[1,2] **Chunming He**[4]
Xiu Li[1,†] **Minfeng Xu**[2,3,†]
[1]Tsinghua University [2]DAMO Academy, Alibaba Group [3]Hupan Lab [4]Duke University

ABSTRACT

Multimodal large language models are promising for clinical visual question answering tasks, but scaling to 3D imaging is hindered by high computational costs. Prior methods often rely on 2D slices or fixed-length token compression, disrupting volumetric continuity and obscuring subtle findings. We present Photon[1], a framework that represents 3D medical volumes with token sequences of variable length. Photon introduces instruction-conditioned token scheduling and surrogate gradient propagation to adaptively reduce tokens during both training and inference, which lowers computational cost while mitigating the attention dilution caused by redundant tokens. It incorporates a custom backpropagation rule with gradient restoration to enable differentiable optimization despite discrete token drop. To stabilize token compression and ensure reliable use of visual evidence, Photon further applies regularization objectives that mitigate language-only bias and improve reliability. Experiments on diverse medical visual question answering tasks show that Photon achieves state-of-the-art accuracy while reducing resource usage and accelerating both training and inference.

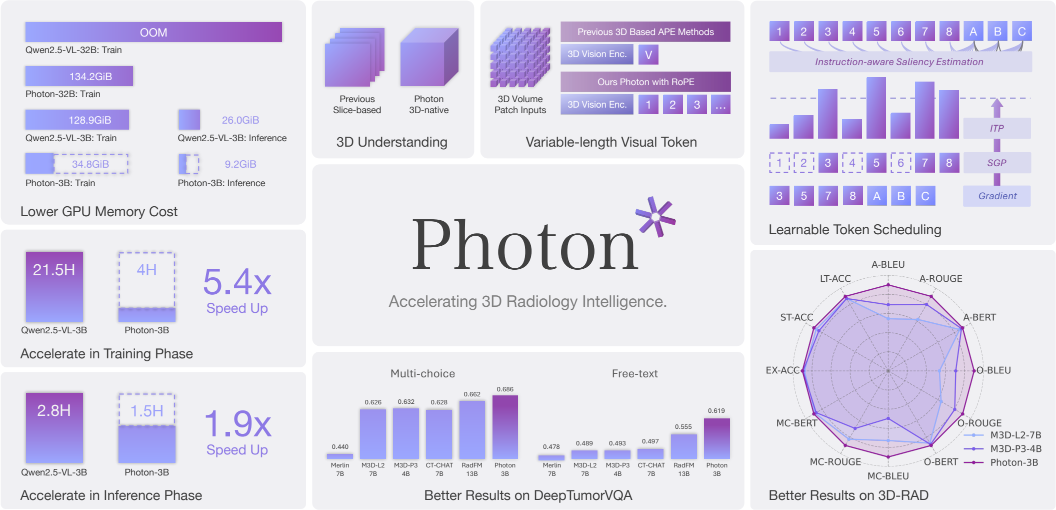

Figure 1: Photon is a 3D-native framework that adaptively models medical volumes using variable-length tokens, accelerating both training and inference. It enables efficient clinical question answering by removing instruction-irrelevant tokens while maintaining better quantitative performance.

[*] Equal Contribution, † Corresponding Author. This work was done during Chengyu Fang and Zheng Jiang's internship at DAMO Academy, Alibaba Group. Email: chengyufang.thu@gmail.com

[1] Photon: the quantum particle of light in nature and the fundamental component of X-rays in CT. Its speed, controllable energy deposition, and discrete interactions for precise measurement align well with our core idea.

1 Introduction

Recent advances in multimodal large language models (MLLMs) open new directions for clinical question answering. Despite these advances, modeling entire 3D volumes remains challenging because of heavy memory and computational demands. To reduce cost, many systems adopt slice-based pipelines or select a limited set of frames from CT or MRI scans (Xu et al., 2025; Chen et al., 2024a; Sellergren et al., 2025; Li et al., 2023a). Although such strategies shorten input sequences, they disrupt spatial continuity, eliminate volumetric detail, and introduce human bias in frame selection.

To preserve volumetric fidelity without manual frame selection, reducing visual tokens has become a promising strategy. In the general domain, approaches such as VisionZip (Yang et al., 2025d) and LLaVA-PruMerge (Shang et al., 2024) prune or merge tokens directly based on attention or similarity, achieving a speed-up in the inference time. However, these methods uniformly apply saliency signals without instruction awareness, making them prone to discarding subtle but clinically important patterns. Moreover, most employ fixed pruning ratios, limiting flexibility in instruction-conditioned tasks. ATP-LLaVA (Ye et al., 2025) introduces learnable thresholds for adaptive pruning, but still retains soft masks during training, so computation and memory are not reduced until inference.

In the medical domain, recent studies have advanced MLLMs toward volumetric modeling by aligning 3D vision encoders with large language models (Wu et al., 2023; Bai et al., 2024; Hamamci et al., 2024b; Blankemeier et al., 2024). These models support joint reasoning over full 3D volumes and alleviate some limitations of 2D slice-based inputs. However, they often produce visual embeddings in a few and fixed length, limiting high-resolution detail preservation and spatial interpretability.

To address these limitations, we propose Photon, a native 3D MLLM framework to model 3D medical volumes with variable-length token sequences, preserving volumetric fidelity without slice sampling or fixed-length token compression. Photon integrates two complementary components: Instruction-conditioned Token Scheduling (ITS) and Surrogate Gradient Propagation (SGP). ITS adaptively reduces visual tokens by estimating instruction-aware saliency and predicting instance-specific thresholds. SGP enables effective training by restoring gradients to retention probabilities, ensuring that token selection remains differentiable and instruction-driven. In the forward pass, Photon removes unimportant tokens together with their caches and positional encodings to lower computation. In the backward pass, a straight-through surrogate mask restores gradients to the underlying retention probabilities, allowing optimization to reflect instruction-driven token importance. To further enhance stability, Photon incorporates lightweight regularization objectives that mitigate language-only hallucination bias and improve reliability.

The main contributions of this work are summarized as follows:

(1) We present Photon, a medical multimodal large language model that directly operates on 3D scans and produces variable-length token sequences, preserving critical volumetric details without slice sampling or fixed token compression ratio.

(2) We introduce Instruction-conditioned Token Scheduling (ITS), which leverages instruction self-affinity and instruction-vision interactions to adaptively regulate visual token retention.

(3) We propose Surrogate Gradient Propagation (SGP), a mechanism that combines discrete token reduction in the forward pass with surrogate gradient optimization in the backward pass, enabling differentiable training despite discrete token dropping.

(4) Photon significantly accelerates both training and inference compared to general-purpose MLLMs, while achieving state-of-the-art performance on multiple medical visual question answering tasks.

2 Related Work

Medical Vision-Language Models. Early medical VLMs, such as BiomedGPT (Luo et al., 2023) and CT2Rep (Hamamci et al., 2024a), primarily adopted CLIP-style alignment between 2D slices and text, but lacked scalability and capability of interactive reasoning. More recent MLLM models have also been adapted to the medical tasks, inspiring systems such as HealthGPT (Lin et al., 2025a), Med-R1 (Lai et al., 2025), and others (Li et al., 2023a; Sellergren et al., 2025; Pan et al., 2025). Most of these methods retain the slice-based paradigm, which undermines volumetric context and risks spatial discontinuity. To enhance spatial understanding, volumetric MLLMs (Lee et al., 2024) such

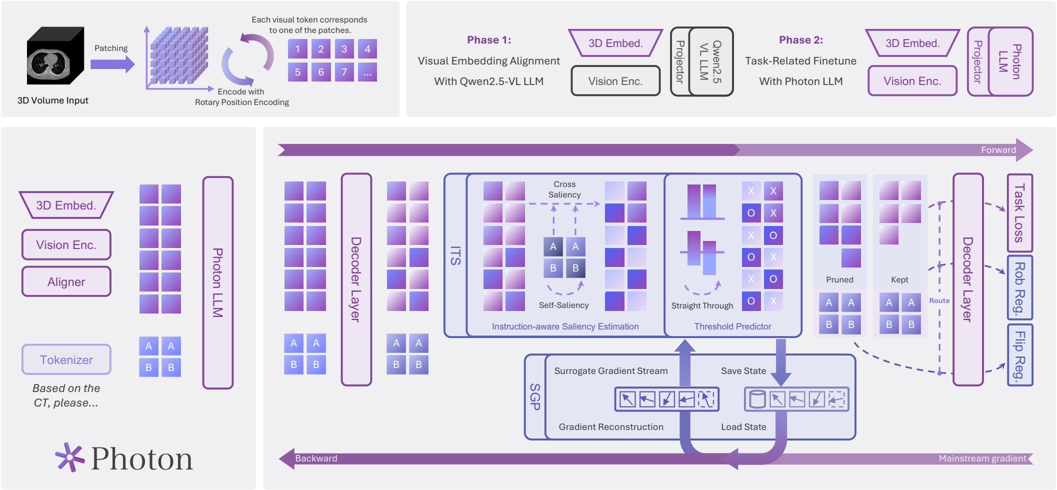

Figure 2: Photon's pipeline: Phase 1 aligns the visual embedding layer, and Phase 2 finetunes all modules for task adaptation, learning token reduction threshold estimation through our backpropagation strategy. Modules in right upper with black contour are not updated during training.

as RadFM (Wu et al., 2023) and M3D (Bai et al., 2024) align 3D vision encoders with language models, but compress each scan into a fixed-length sequence of vision tokens. The sequence length is typically small due to memory constraints, limiting their scalability to high-resolution inputs and weakening fine-grained spatial detail. OmniV-Med (Jiang et al., 2025) instead supports variable-length sequences, but its pruning strategy relies on L1 similarity of slice features, a coarse criterion that can inadvertently remove subtle, yet clinically important pathologies.

Visual Token Reduction. To lower computational cost in large vision-language models, many works compress the visual representation at the vision-language interface or within vision encoder layers. Representative designs include Q-Former (Li et al., 2023b), clustering-based merging (Shang et al., 2024), and pooling modules (Li et al., 2024b; Yao et al., 2024), as well as internal pruning that removes less informative tokens inside the model (Chen et al., 2024b). Although these approaches reduce token redundancy and improve efficiency, they ignore that different instructions require different amounts of information. In medical imaging, diverse instructions often focus on distinct anatomical regions represented by visual token sequences of varying lengths. Therefore, there is a pressing need for adaptive token reduction strategies tailored to computationally intensive scenarios. IVTP (Huang et al., 2024), TransPrune (Li et al., 2025a) and some pioneering works (Han et al., 2024; Wang et al., 2024b; Xing et al., 2024; Zhang et al., 2025a;c; Dhouib et al., 2025) sort the visual tokens by heuristic methods (Yang et al., 2025d; Alvar et al., 2025; Zhang et al., 2025d; Yang et al., 2025b; Sun et al., 2025) to enhance the relevance between visual token reduction and instructions. These methods account for instruction-vision correlation but are restricted to fixed retention ratios or manually set thresholds, which risks discarding vital pathological cues in medical imaging. ATP-LLaVA (Ye et al., 2025) introduces learnable thresholds to enable adaptive pruning but applies pruning only at inference, while additional computational cost is still required during training.

3 Methodology

Photon is a multimodal framework that integrates a 3D vision encoder with a large language model to jointly process volumetric scans and clinical instructions (see Fig. 2). It directly models entire medical volumes by partitioning them into 3D patches and mapping each patch to a token. The token sequence length is dynamically adjusted to balance spatial detail preservation against computational cost while mitigating the attention dilution caused by redundant tokens. **In the forward computation**, visual tokens are adaptively reduced according to their estimated importance and the predicted threshold derived from the visual summaries. **In the backward computation**, discrete selection remains differentiable through a straight-through path with masked gradient routing aligned to the active tokens, ensuring the same selection logic is honored in both training and inference.

3.1 Input Processing and 3D Vision Encoder

Given an input scan of size $D \times H \times W$, the volume is divided into non-overlapping $14 \times 14 \times 14$ patches. Each patch is linearly embedded into a d-dimensional vector. To balance resolution and sequence length, spatial merging is applied only along (H, W) with stride S, while the depth D remains unchanged. The compact grid contains visual tokens with a length of:

$$N_v \;=\; D \cdot \tfrac{H'}{S} \cdot \tfrac{W'}{S}, \tag{1}$$

where H' and W' are the in-plane sizes after patchification. Let $\mathcal{V} = \{1, \ldots, N_v\}$ be the visual-token index set and $\mathcal{Q} = \{1, \ldots, N_t\}$ be the instruction-token index set. Our 3D vision encoder (ViT-based) then handles the full visual-token set $\mathcal{V}$, and encodes these tokens into visual embeddings $\mathrm{T}_{\mathrm{vis}}$ in the same hidden dimension of $\mathrm{T}_{\mathrm{txt}}$ that is encoded by a language tokenizer. Photon's LLM decoder part takes as input the following hybrid tokens:

$$\mathrm{T}^0 \;=\; [\,\mathrm{T}^0_{\mathrm{vis}},\; \mathrm{T}^0_{\mathrm{txt}}\,], \tag{2}$$

with positional indices following Qwen2.5-VL (Bai et al., 2025). Tokens are processed by self-attention and feed-forward blocks. To improve efficiency under instructions, Surrogate Gradient Propagation (SGP) is applied at selected layer $\ell \in \ell_n$ of Photon's language modules.

3.2 Instruction-conditioned Token Scheduling

Token-level saliency scores provide a relative ranking of visual tokens within each sample, but do not specify how many tokens should be retained in total. A fixed retention ratio would treat all scans and instructions equally, ignoring differences in complexity and clinical focus implied by instructions. To address this, we introduce Instruction-conditioned Token Scheduling (ITS), a mechanism that adapts the pruning threshold to each sample by conditioning on both the instruction and the token-level distribution. ITS integrates the Instruction-aware Saliency Estimation (ISE) rule with an Instance-aware Threshold Predictor (ITP), ensuring that token retention adapts to instruction demands while maintaining visual compactness.

Instruction-aware Saliency Estimation. To estimate the saliency of visual tokens under instruction guidance, we introduce an ISE at a selection layer $\ell \in \ell_n$, which explicitly links token saliency to variations in the given instructions.

Let q_t denote the query vector of the t-th instruction token, $k_{t'}$ the key vector of the t'-th instruction token ($t, t' \in \mathcal{Q}$), and α the dimensions of the attention head. To prevent trivial self-matching, we exclude the diagonal ($t' = t$) and define the centrality score as:

$$c_t \;=\; \sum_{t' \in \mathcal{Q}} \max\Big(\frac{\langle q_t, k_{t'} \rangle}{\sqrt{\alpha}},\, 0\Big), \tag{3}$$

which measures the extent to which token t is positively reinforced by other instruction tokens, while ignoring negative contributions. The centralities are then normalized into weights:

$$w_t \;=\; \frac{c_t}{\sum_{t' \in \mathcal{Q}} c_{t'}}, \qquad \sum_{t \in \mathcal{Q}} w_t = 1, \tag{4}$$

where the tokens with consistently strong positive affinities obtain larger w_t, thereby highlighting salient instruction tokens that contribute more to the results. Let k_j denote the key vector of the j-th ($j \in \mathcal{V}$) visual token, we compute the weighted instruction-visual saliency score by:

$$\rho_j \;=\; \mathrm{norm}(u_j), \qquad u_j = \sum_{t \in \mathcal{Q}} w_t \,\frac{\langle q_t, k_j \rangle}{\sqrt{\alpha}}, \qquad \rho_j \in [0, 1], u_j \in [-\infty, +\infty] \tag{5}$$

where $\mathrm{norm}(\cdot)$ denotes instance-wise min-max normalization. The saliency score ρ_j, reflecting how strongly each visual token aligns with the most central instruction tokens, provides a relative importance ranking that serves as the basis for adaptive thresholding.

Instance-aware Thresholding Prediction. While saliency scores provide token-wise rankings, they do not determine the retention level per instance. A fixed keep ratio ignores variability in scan complexity and instruction demands.

To adapt retention, Photon introduces ITP to predict an instance-specific threshold conditioned on both the instruction and the distribution of visual saliency scores. According to the results of ISE, $u = \{u_j\}_{j \in \mathcal{V}}$ is the raw logits and $\rho = \{\rho_j\}_{j \in \mathcal{V}}$ is the normalized scores. We construct a feature vector from three complementary views:

$$z = [\,\Psi(\rho),\ \Phi(u),\ \Upsilon(u)\,], \tag{6}$$

where Ψ, Φ, Υ summarize distributional shape, absolute scale, and compressed tails, respectively (see Appendix A.1.2). We combine these to form a compact descriptor z. A lightweight predictor then maps z to a scalar threshold:

$$\theta \;=\; \sigma\bigl(W_2\,\phi(W_1 z + b_1) + b_2\bigr), \qquad \theta \in [0,1], \tag{7}$$

where (W_1, b_1) and (W_2, b_2) denote the weight-bias pairs of the hidden and output layers, ϕ is the GELU activation, and σ is the logistic function. The resulting θ serves as a smooth probabilistic threshold, which can be directly compared with the normalized saliency ρ_j:

$$q_j \;=\; \sigma\Bigl(\tfrac{\rho_j - \theta}{\tau_{\text{ce}}}\Bigr), \qquad q_j \in [0,1], \tag{8}$$

where the q_j denotes the retention probability and τ_{ce} is a sufficiently small coefficient to make the continuous mask approximate to binary. Based on this sigmoid result, we split to get the token retention binary mask with:

$$M_j = \mathbf{1}\{\,q_j > 0.5\,\}, \tag{9}$$

Tokens with $M_j = 0$ are hard dropped and removed entirely, including their cache, attention mask, and positional embedding. To enable differentiability, we replace M with a straight-through surrogate:

$$\widetilde{M} = \text{sg}(M) - \text{sg}(q) + q, \tag{10}$$

where $\text{sg}(\cdot)$ denotes the stop-gradient operator, and $q = \{q_j\}_{j \in \mathcal{V}}$. Thus the forward path follows hard selection, while the backward path propagates gradients through probabilities. The surrogate gradients that govern the update dynamics are detailed in the subsequent forward-backward analysis.

3.3 Surrogate Gradient Propagation

Instruction-conditioned Token Scheduling (ITS) produces the surrogate mask $\widetilde{M}$ that determines which tokens are retained in the forward sequence. Surrogate Gradient Propagation (SGP) addresses the training challenge that arises from this discrete selection by restoring gradients to the retained tokens and by providing surrogate gradients for the retention probabilities derived from the threshold predictor. Specifically, the upstream gradient of the compressed sequence is scattered back to the original tokens as:

$$\frac{\partial \mathcal{L}}{\partial \mathrm{T}^{\ell}_{\text{vis}}} = \mathcal{S}\Bigl(\tfrac{\partial \mathcal{L}}{\partial {\mathrm{T}^{\ell}_{\text{vis}}}'};\, \widetilde{M}\Bigr)\,, \tag{11}$$

where $\mathcal{S}(\cdot; \widetilde{M})$ scatters gradients from the compressed sequence ${\mathrm{T}^{\ell}_{\text{vis}}}'$ back to their original positions in $\mathrm{T}^{\ell}_{\text{vis}}$. This scattered path keeps decoder activations trainable for retained tokens. However, the threshold predictor receives no useful optimization signal, since the hard selection operation blocks gradients with respect to its probabilities. To address this, we design a surrogate gradient on q_j so that the predictor can be optimized under token pruning.

With token-level gradients available, we define an importance score that measures the task-driven contribution of each token. Saliency scores ρ_j and retention probabilities q_j characterize relevance or selection tendency, but they do not reflect the effect of tokens on the loss. We therefore adopt a first-order approximation, where the variation in loss induced by removing a token is estimated by the inner product between its activation and gradient (detailed in Appendix A.1.4):

$$\eta_j = \Bigl\langle (\mathrm{T}^{\ell}_{\text{vis}})_j,\ \bigl(\tfrac{\partial \mathcal{L}}{\partial \mathrm{T}^{\ell}_{\text{vis}}}\bigr)_j \Bigr\rangle. \tag{12}$$

Here η_j reflects the contribution of token j to the loss, with larger values indicating stronger influence. These scores are standardized and clipped:

$$z_j = \frac{\eta_j - \mu(\eta \odot \widetilde{M})}{\max\{\text{Std}(\eta \odot \widetilde{M}),\, \epsilon_{\text{std}}\}}, \qquad z_j \leftarrow \text{clip}(z_j,\, -c,\, c), \tag{13}$$

where $\mu(\cdot)$ and $\mathrm{Std}(\cdot)$ denote the masked mean and standard deviation, ϵ_{std} prevents division by small variance, and c bounds outliers. The standardized values are rescaled into $(0, 1)$ through a smooth monotonic mapping $\psi(\cdot)$. The directional term is then defined as:

$$r_j = \psi(z_j), \qquad d_j = 0.5 - \mathrm{sg}(r_j), \tag{14}$$

where $\psi(0) = 0.5$ serves as the neutral point, so that d_j quantifies the deviation from this midpoint. In parallel, a magnitude factor is computed by accumulating activation-gradient products across the feature dimension:

$$m_j = \sum_{k=1}^{d} \left|(\mathrm{T}_{\text{vis}}^{\ell})_{jk}\, g_{jk}\right|, \qquad g_j = \left(\frac{\partial \mathcal{L}}{\partial \mathrm{T}_{\text{vis}}^{\ell}}\right)_j, \tag{15}$$

where $(\mathrm{T}_{\text{vis}}^{\ell})_{jk}$ and g_{jk} are the k-th components of $(\mathrm{T}_{\text{vis}}^{\ell})_j$ and g_j. These values are normalized within each row and clamped to a bounded interval:

$$s_j = \mathrm{clip}\left(\frac{m_j}{\mu_{\text{row}}(m \odot \widetilde{M}) + \varepsilon},\, s_{\min},\, s_{\max}\right), \tag{16}$$

which yields a scale factor that amplifies consistently strong activation-gradient interactions while suppressing weak ones. Finally, combining direction and magnitude provides the surrogate gradient with respect to the relaxed probabilities:

$$\frac{\partial \mathcal{L}}{\partial q_j} \;\approx\; \beta\, d_j\, s_j\, \max\{q_j(1 - q_j),\, \epsilon_{sat}\}. \tag{17}$$

where β balances directional and magnitude contributions, $\epsilon_{sat} > 0$ provides a lower bound on the gradient term $q_j(1 - q_j)$ to avoid vanishing when q_j is close to 0 or 1, thereby ensuring stable updates. As a result, tokens assessed as more informative are gradually reinforced toward retention, whereas less informative tokens are progressively suppressed, which guarantees that the pruning mechanism behaves as intended (see detailed analysis in Appendix A.1.3).

3.4 Objective

Soft Retention Band. While forward-backward learning already propagates supervision to guide pruning, unconstrained training may converge to degenerate cases of keeping nearly all or pruning excessively. To avoid such extremes, we constraint the retention probabilities q_j by softly constraining their mean ratio r within a band:

$$\mathcal{L}_{\text{band}} = \mathbb{E}[\max(0, r - r_{\max}) + \max(0, r_{\min} - r)]\,, \qquad r = \tfrac{1}{N_v}\sum_{j \in \mathcal{V}} q_j, \tag{18}$$

This band-constrained penalty softly restricts the retention ratio to a stable range, ensuring pruning remains effective without overriding the dynamics of the forward-backward process.

Robustness Regularizer. Another failure mode in multimodal learning is language-only hallucination bias, where answers rely on textual priors while ignoring the image. This risk is critical in medical tasks, since predictions may appear correct without visual grounding. To address it, the model is encouraged to produce higher predictive uncertainty whenever visual evidence is insufficient. Given a perturbed volume $\tilde{x}$ (by masking, shuffling, etc.), the robustness loss is defined as:

$$\mathcal{L}_{\text{robust}} = -\,\mathbb{E}_{\tilde{x}}[H(p_\theta(\cdot|\tilde{x}))]\,, \qquad H(p) = -\sum_{v} p(v)\log p(v). \tag{19}$$

During these perturbed cases, we drop other loss functions and optimize only $\mathcal{L}_{\text{robust}}$. This discourages overconfident predictions without valid visual grounding.

Flip Regularizer. To further reduce reliance on spurious pruning patterns, we introduce a mask-flip regularizer. With a certain probability, the retention mask is inverted so that tokens originally reduced are retained and those originally retained are reduced. Under this adversarial mask, the model should not remain highly confident on the correct answer; otherwise, it indicates over-reliance on textual priors or shortcut cues. We penalize such cases by assigning a higher loss whenever the model still predicts the correct label with high confidence:

$$\mathcal{L}_{\text{flip}} = -\,\mathbb{E}_{\widetilde{M}^{\text{flip}}}\left[\log\!\left(1 - p_\theta(y \mid x, \widetilde{M}^{\text{flip}}) + \epsilon\right)\right], \tag{20}$$

Table 1: Comparison of zero-shot and finetuned performance across six tasks in 3D-RAD benchmark. **violet** and **indigo** indicate the best and the second best. Stat. Temp. Diag. = Static Temporal Diagnosis, Longit. Temp. Diag. = Longitudinal Temporal Diagnosis.

Task	**Metric**	**Zero-shot**						**Finetuned**		
		Qwen2.5-VL	RadFM	M3D-L2	M3D-P3	OmniV	Lingshu	M3D-L2	M3D-P3	Photon
		3B	13B	7B	4B	1.5B	7B	7B	4B	3B
Existence Detection	Accuracy	19.52	29.20	18.00	**40.25**	28.66	**59.60**	81.09	**82.43**	**83.07**
Stat. Temp. Diag.	Accuracy	0.00	**44.11**	**25.47**	25.40	22.96	6.02	**51.20**	49.30	**52.86**
Longit. Temp. Diag.	Accuracy	0.29	**42.99**	24.17	**24.31**	24.23	12.13	**74.78**	74.77	**77.01**
Medical Measurement	BLEU	1.78	**3.34**	**15.95**	2.55	2.52	2.50	30.54	**33.52**	**37.74**
	ROUGE	4.30	6.62	**23.24**	5.63	**7.88**	5.45	36.06	**36.46**	**39.36**
	BERT Score	84.20	**86.85**	**91.50**	85.74	85.66	83.81	94.65	**94.86**	**96.14**
Image Observation	BLEU	3.51	13.48	10.69	**16.31**	**16.42**	5.34	31.28	**39.66**	**51.59**
	ROUGE	8.84	19.14	20.82	**23.19**	**26.69**	12.25	39.12	**50.52**	**56.66**
	BERT Score	84.53	**87.16**	86.61	86.92	**88.29**	85.67	90.00	**92.19**	**93.62**
Anomaly Detection	BLEU	2.93	11.00	9.10	**15.06**	**13.47**	3.71	25.25	**33.28**	**42.33**
	ROUGE	9.17	17.62	18.64	**23.19**	**25.72**	9.46	33.76	**42.45**	**47.50**
	BERT Score	84.47	86.76	86.07	**87.11**	**88.21**	84.81	89.16	**90.72**	**91.96**

where $p_\theta(y \mid x, \widetilde{M}^{\text{flip}})$ is the probability of the ground-truth label under the flipped mask and ϵ is a small constant for numerical stability. This regularizer discourages the model from producing correct answers under inconsistent retention, thereby reinforcing reliance on the intended pruning structure.

Overall Objective. In training Phase 1, we only use the cross-entropy loss to supervise the alignment. In training Phase 2, the complete training objective combines faithful language modeling, stable token usage, robustness against language-only hallucination bias, and consistency under mask flipping:

$$\mathcal{L} = (\mathcal{L}_{\text{CE}} \text{ or } \mathcal{L}_{\text{band}} \text{ or } \mathcal{L}_{\text{robust}}) + \mathcal{L}_{\text{flip}}, \qquad \mathcal{L}_{\text{CE}} = -\,\mathbb{E}_{(x,y)}\left[\log p_\theta(y|x)\right]. \tag{21}$$

This innovative design ensures that Photon learns to generate clinically accurate text, maintains efficiency through adaptive token pruning, and grounds its reasoning on volumetric evidence rather than spurious textual patterns.

4 Experiments

All comparison baselines are initialized from models that have been pretrained or finetuned on large-scale medical datasets and then further finetuned following their respective protocols. In contrast, before task-specific finetuning, our method applies only a lightweight alignment of the 3D vision patch embedding layer using volume-caption pairs while keeping the ViT backbone, MLP aligner, and LLM decoder frozen. Details of the training process (Appendix A.1.1), experimental setup (Appendix A.2.1), and dataset information (Appendix A.2.2) are provided in the appendix.

4.1 Comparative Evaluation

On 3D-RAD (Gai et al., 2025), Photon achieves the best finetuned results across all tasks in Table 1. The most notable gains appear in anomaly detection and image observation, where performance improves by about 14.0% compared with the best baseline. Medical measurement also shows a clear improvement of about 7.3%, which is critical since measurement accuracy directly underpins many downstream diagnostic decisions. Longitudinal temporal diagnosis rises by around 3.0%. These results highlight Photon's ability to retain volumetric details and adjust token selection based on instruction relevance, thereby enhancing the accuracy of both descriptive and quantitative clinical predictions. The consistent improvements across descriptive (e.g., anomaly detection, observation), quantitative (e.g., measurement), and reasoning-oriented (e.g., temporal diagnosis) tasks indicate that Photon generalizes beyond a single evaluation type.

On DeepTumorVQA (Chen et al., 2025c), Photon also obtains the highest overall accuracy in both multi-choice and free-text settings in Table 2. The total average in multi-choice increases by about 3.6%, while in free-text the improvement is larger at approximately 11.5%. The strongest gains occur in measurement subtypes evaluated with MRA, where Photon improves by more than 35.3%, confirming its strength in handling numerical and quantitative queries. Visual reasoning subtypes,

Table 2: Performance on DeepTumorVQA benchmark. Subtypes marked with * indicate free-text numerical answers evaluated using MRA, higher is better. Meas. = Measurement, Recog. = Recognition, Vis. Rsn. = Visual Reasoning, Med. Rsn. = Medical Reasoning.

Type	Subtype	Multi-choice							Free-text					
		Rand	Merlin	M3D-L2	M3D-P3	CT-CHAT	RadFM	Photon	Merlin	M3D-L2	M3D-P3	CT-CHAT	RadFM	Photon
		—	7B	7B	4B	7B	13B	3B	7B	7B	4B	7B	13B	3B
Meas.	lesion volume measurement*	0.250	0.253	0.815	0.825	0.833	0.815	0.825	0.079	0.085	0.079	0.075	0.112	0.265
	organ HU measurement*	0.250	0.254	0.638	0.640	0.637	0.647	0.642	0.487	0.490	0.491	0.513	0.608	0.777
	organ volume measurement*	0.250	0.262	0.747	0.754	0.750	0.755	0.756	0.526	0.535	0.528	0.549	0.583	0.717
	Average	0.250	0.256	0.733	**0.740**	**0.740**	0.739	**0.741**	0.364	0.370	0.366	0.379	**0.434**	**0.587**
Recog.	colon lesion existence	0.500	0.859	0.859	0.859	0.859	0.856	0.858	0.859	0.859	0.859	0.859	0.893	0.881
	kidney cyst existence	0.500	0.797	0.797	0.797	0.797	0.861	0.910	0.797	0.797	0.797	0.797	0.864	0.917
	kidney lesion existence	0.500	0.495	0.510	0.501	0.514	0.668	0.717	0.511	0.515	0.490	0.507	0.692	0.624
	kidney tumor existence	0.500	0.564	0.574	0.574	0.574	0.886	0.896	0.574	0.574	0.574	0.574	0.890	0.895
	liver lesion existence	0.500	0.535	0.524	0.517	0.524	0.652	0.681	0.524	0.524	0.524	0.524	0.662	0.640
	pancreatic lesion existence	0.500	0.718	0.718	0.718	0.718	0.810	0.805	0.718	0.718	0.718	0.718	0.871	0.819
	Average	0.500	0.661	0.664	0.661	0.664	**0.789**	**0.811**	0.664	0.665	0.660	0.663	**0.812**	**0.796**
Vis. Rsn.	adjacent organ	0.333	0.217	0.565	0.609	0.609	0.609	0.696	0.174	0.174	0.304	0.304	0.435	0.304
	inter-segment comparison	0.333	0.470	0.567	0.576	0.572	0.591	0.549	0.577	0.561	0.592	0.589	0.456	0.359
	kidney volume comparison	0.333	0.347	0.370	0.364	0.372	0.386	0.370	0.350	0.370	0.356	0.370	0.386	0.396
	largest lesion attenuation	0.333	0.317	0.541	0.539	0.544	0.555	0.539	0.526	0.544	0.548	0.542	0.521	0.571
	largest lesion diameter*	0.250	0.263	0.778	0.783	0.781	0.766	0.776	0.182	0.209	0.233	0.269	0.232	0.310
	largest lesion location	0.392	0.307	0.310	0.310	0.340	0.340	0.356	0.359	0.353	0.337	0.353	0.334	0.350
	largest lesion slice*	0.250	0.241	0.672	0.684	0.672	0.664	0.703	0.524	0.533	0.510	0.513	0.672	0.723
	lesion count by location*	0.250	0.583	0.861	0.860	0.862	0.861	0.865	0.534	0.534	0.534	0.534	0.506	0.546
	lesion counting*	0.328	0.455	0.781	0.784	0.796	0.790	0.985	0.000	0.000	0.000	0.000	0.001	0.917
	lesion outlier	0.500	0.521	0.507	0.549	0.451	0.493	0.535	0.451	0.535	0.535	0.577	0.521	0.634
	liver lesion clustering	0.333	0.331	0.438	0.475	0.463	0.469	0.475	0.388	0.469	0.469	0.431	0.513	0.456
	organ aggregation*	0.250	0.257	0.660	0.667	0.655	0.661	0.660	0.577	0.569	0.586	0.574	0.621	0.798
	organ enlargement	0.500	0.736	0.736	0.736	0.736	0.746	0.791	0.736	0.736	0.736	0.736	0.759	0.845
	tumor organ HU difference*	0.305	0.296	0.836	0.839	0.821	0.821	0.829	0.113	0.122	0.139	0.197	0.189	0.207
	Average	0.335	0.382	0.616	**0.627**	0.620	0.625	**0.653**	0.392	0.408	0.420	0.428	**0.439**	**0.530**
Med. Rsn.	fatty liver	0.333	0.318	0.461	0.455	0.481	0.481	0.558	0.481	0.481	0.396	0.487	0.578	0.773
	lesion type classification	0.500	0.865	0.865	0.865	0.865	0.865	0.865	0.865	0.865	0.865	0.865	0.851	0.865
	pancreatic cyst resectability	0.500	0.371	0.657	0.800	0.800	0.771	0.771	0.800	0.800	0.800	0.800	0.771	0.743
	pancreatic lesion resectability	0.333	0.379	0.483	0.483	0.483	0.483	0.483	0.414	0.483	0.483	0.483	0.483	0.483
	pancreatic steatosis	0.500	0.526	0.526	0.513	0.513	0.579	0.526	0.526	0.526	0.526	0.526	0.658	0.671
	pancreatic tumor staging	0.250	0.216	0.351	0.243	0.189	0.324	0.460	0.216	0.216	0.297	0.135	0.432	0.460
	Average	0.403	0.446	0.557	0.560	0.555	**0.584**	**0.611**	0.550	0.562	0.561	0.549	**0.629**	**0.666**
	Total Average	0.369	0.440	0.626	0.632	0.628	**0.662**	**0.686**	0.478	0.489	0.493	0.497	**0.555**	**0.619**

such as lesion counting and slice localization, also show large margins exceeding 20.7%, reflecting better spatial understanding. These large improvements in both measurement and reasoning tasks suggest that Photon is not only effective for recognition but also excels in tasks that require quantitative precision and spatial analysis. Taken together, the results from both 3D-RAD and DeepTumorVQA confirm that Photon delivers consistent and meaningful benefits in multiple tasks, strengthening its reliability as a versatile medical vision-language system.

4.1.1 Comparative Evaluation with Token Pruning Methods

Most existing pruning methods for multimodal large language models do not provide case-specific adaptive retention based on instruction-related visual content. Instead, they typically rely on fixed retention ratios. To fairly compare with such methods, we follow their configurations and evaluate them at three nominal retention levels (about 30%, 50%, and 70% of visual tokens), which correspond to keeping roughly 2.1K, 3.5K, and 4.9K vision tokens per sample in our 3D-RAD setup.

It is also important to note that these methods were not designed to optimize training-time acceleration, backpropagation stability, or overall training robustness. Several of them do not provide a complete training recipe. In the 3D medical setting, where the base model has limited prior knowledge and relies heavily on visual evidence, directly training with such pruning strategies can lead to premature removal of important tokens and a collapse towards language-only bias. To avoid this issue and keep the comparison fair, we first train a full Qwen2.5-VL model without pruning using the paradigms recommended in the respective papers, and then apply the pruning methods only at inference time using their official code. This isolates the effect of pruning at prediction time and avoids confounding factors from unstable training.

Most previous pruning methods, including VisionZip (Yang et al., 2025d) and HiPrune (Liu et al., 2025b), are not optimized for compatibility with FlashAttention in the visual encoder or require extra attention computation across all visual encoder layers. This leads to additional overhead and erodes the expected speed gains. In our setting, which has a large number of visual tokens and relatively short textual answers, these methods do not provide clear advantages in inference speed, HiPrune (Liu et al., 2025b) in particular slows down decoding despite keeping fewer tokens. By contrast, Photon couples instruction-conditioned pruning with a FlashAttention-friendly implementation and a pruning

Table 3: Comparison of different token pruning strategies on 3D-RAD. E.D. = Existence Detection, S.T.D. = Static Temporal Diagnosis, L.T.D. = Longitudinal Temporal Diagnosis.

Methods	E.D.	S.T.D.	L.T.D.	Medical Measurement			Image Observation			Anomaly Detection			Infer Speed	Token Num
	Acc.	Acc.	Acc.	BLEU	ROUGE	BERT	BLEU	ROUGE	BERT	BLEU	ROUGE	BERT	(Tok/s)	(Tok/case)
Qwen2.5-VL	81.97	47.62	75.36	37.00	38.57	96.04	52.72	56.48	93.63	42.01	47.36	91.93	2.30	7.0K
VisionZip	82.00	47.19	75.42	37.04	38.69	96.06	52.51	56.36	93.63	41.96	47.39	91.93	2.32	2.1K
VisionZip	81.99	47.74	75.93	37.11	38.68	96.07	52.72	56.60	93.65	41.98	47.36	91.92	2.23	3.5K
VisionZip	82.01	47.40	75.88	37.07	38.82	96.04	52.57	56.43	93.64	42.01	47.39	91.93	2.18	4.9K
HiPrune	81.99	48.08	75.50	37.00	38.59	96.05	52.56	56.46	93.64	42.08	47.32	91.93	0.76	2.1K
HiPrune	81.97	47.84	75.58	37.14	38.75	96.07	52.65	56.60	93.63	41.92	47.31	91.91	0.75	3.5K
HiPrune	82.02	47.19	75.35	37.00	38.62	96.06	52.57	56.44	93.62	41.94	47.40	91.91	0.73	4.9K
Photon	83.07	52.86	77.01	37.74	39.36	96.14	51.59	56.66	93.62	42.33	47.50	91.96	4.12	Dynamic
Photon MAX	85.50	57.79	79.70	39.44	40.96	96.17	52.83	58.72	93.70	42.85	48.89	92.00	2.60	Dynamic

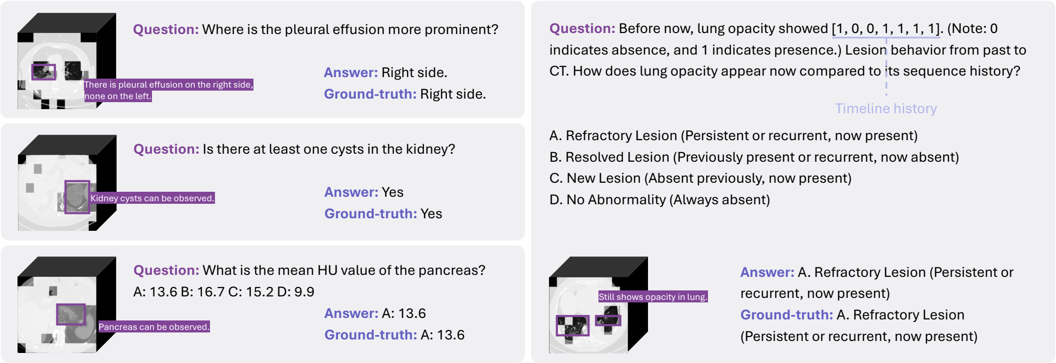
There is pleural effusion on the right side, none on the left.
Kidney cysts can be observed.
Pancreas can be observed.
Timeline history
Still shows opacity in lung.

Question: Where is the pleural effusion more prominent?

Answer: Right side.
Ground-truth: Right side.

Question: Is there at least one cysts in the kidney?

Answer: Yes
Ground-truth: Yes

Question: What is the mean HU value of the pancreas?
A: 13.6 B: 16.7 C: 15.2 D: 9.9

Answer: A: 13.6
Ground-truth: A: 13.6

Question: Before now, lung opacity showed [1, 0, 0, 1, 1, 1, 1]. (Note: 0 indicates absence, and 1 indicates presence.) Lesion behavior from past to CT. How does lung opacity appear now compared to its sequence history?

A. Refractory Lesion (Persistent or recurrent, now present)
B. Resolved Lesion (Previously present or recurrent, now absent)
C. New Lesion (Absent previously, now present)
D. No Abnormality (Always absent)

Answer: A. Refractory Lesion (Persistent or recurrent, now present)
Ground-truth: A. Refractory Lesion (Persistent or recurrent, now present)

Figure 3: Visualization of Photon's results. White regions indicate reduced tokens, while purple boxes highlight retained areas that carry clinically relevant information for answering the questions.

schedule that is used during training. As shown in Table 3, Photon achieves higher accuracy on all three 3D-RAD tasks and reaches up to 4.12 tokens/s, improving both performance and inference efficiency under the same backbone.

4.2 Visualization Analysis

Fig. 3 and Fig. 7 show qualitative results of Photon and its token reduction behavior. The examples demonstrate that the model is able to discard large portions of non-essential context while preserving subtle but diagnostically important structures. For instance, when asked about pleural effusion, Photon selectively retains regions around the thoracic cavity, while in kidney cystic-related questions, it keeps the cystic kidney area. These cases indicate that pruning decisions adapt to the clinical focus of each question rather than being uniform. The visual results combined with the results from Table 4 show that our token scheduling process reinforces the contribution of retained tokens, ensuring that relevant regions dominate the final prediction. As a result, Photon maintains high accuracy in various medical visual question answering tasks while reducing redundancy in visual tokens.

4.3 Ablation Study

As shown in Table 4, Photon Phase 1, which finetunes only the modified 3D visual embedding layer, yields clear gains over the zero-shot initialization of Qwen2.5-VL (Bai et al., 2025): BLEU improves by 70% on anomaly detection, 134% on image observation, and existence detection accuracy rises by 44%. These results indicate that re-aligning the adapted 3D patch embedding provides a stronger initialization for subsequent finetuning. To test whether adapting the full vision stack is advantageous, we continued training from the Phase 1 checkpoint. However, even with a small learning rate, fully finetuning the vision encoder and MLP aligner (Vis. Ful. Ft.) led to overfitting and degraded performance. As illustrated in Fig. 4, the model also lost instruction-following capability and often produced answers inconsistent with the given questions.

Table 4: Ablation study on 3D-RAD. Computational statistics include training speed (iterations/s), average retaining tokens, and inference speed (tokens/s), inference peak GPU memory. E.D. = Existence Detection, S.T.D. = Static Temporal Diagnosis, L.T.D. = Longitudinal Temporal Diagnosis.

Task	E.D.	S.T.D.	L.T.D.	Medical Measurement			Image Observation			Anomaly Detection			Computational Metrics			
	Acc.	Acc.	Acc.	BLEU	ROUGE	BERT	BLEU	ROUGE	BERT	BLEU	ROUGE	BERT	Train spd.	Train Tok.	Infer Spd.	Infer Mem.
Without task-related finetune.																
Qwen2.5-VL	19.52	0.00	0.29	1.78	4.30	84.20	3.51	8.84	84.53	2.93	9.17	84.47	—	—	—	—
Vis. Ful. Ft.	0.00	0.00	0.00	5.02	9.91	84.82	1.02	2.96	81.46	0.83	2.61	80.83	—	—	—	—
Photon Phase 1	28.10	8.41	10.90	4.81	9.69	85.35	5.98	17.62	86.39	6.84	15.64	85.98	—	—	—	—
Finetuned with 3D-RAD datasets.																
Qwen2.5-VL Ft.	81.97	47.62	75.36	37.00	38.57	96.04	52.72	56.48	93.63	42.01	47.36	91.93	0.15	7.00K	2.30	26.0GiB
w/o. Photon Phase 1	82.35	52.20	75.69	39.10	40.53	96.17	51.23	56.27	93.55	42.13	47.46	91.92	0.84	0.45K	4.09	9.2GiB
$\ell = 0$	82.09	47.21	75.45	40.29	41.69	96.34	52.18	57.16	93.66	42.12	47.03	91.89	0.82	0.74K	4.03	9.2GiB
$\ell = \ell_{n/2}$	82.23	50.98	76.62	38.08	39.43	96.14	51.94	56.43	93.68	42.05	47.26	91.89	0.84	0.47K	4.09	9.2GiB
$\ell = \ell_{3n/4}$	82.97	52.71	75.86	37.01	38.51	96.06	52.11	56.76	93.64	41.90	47.03	91.87	0.83	0.39K	4.06	9.2GiB
w/o. ITS & SGP	82.40	49.60	75.50	37.60	39.10	96.13	51.60	56.40	93.65	42.10	47.40	91.90	0.64	1.00K	4.03	9.2GiB
w/o. Self-affinity	82.34	52.82	77.89	37.41	38.78	96.05	51.78	55.99	93.67	41.97	47.46	91.91	0.82	0.54K	4.08	9.2GiB
w/o. Robust Reg.	81.81	48.18	77.38	37.54	39.25	95.97	51.70	56.46	93.59	42.05	46.90	91.95	0.87	0.29K	4.14	9.2GiB
w/o. Flip Reg.	82.20	52.09	77.09	36.97	38.24	95.96	51.79	56.61	93.64	42.02	47.50	91.92	0.85	0.38K	4.12	9.2GiB
Photon	83.07	52.86	77.01	37.74	39.36	96.14	51.59	56.66	93.62	42.33	47.50	91.96	0.85	0.39K	4.12	9.2GiB
Photon Max	85.50	57.79	79.70	39.44	40.96	96.17	52.83	58.72	93.70	42.85	48.89	92.00	0.19	3.08K	2.60	21.4GiB

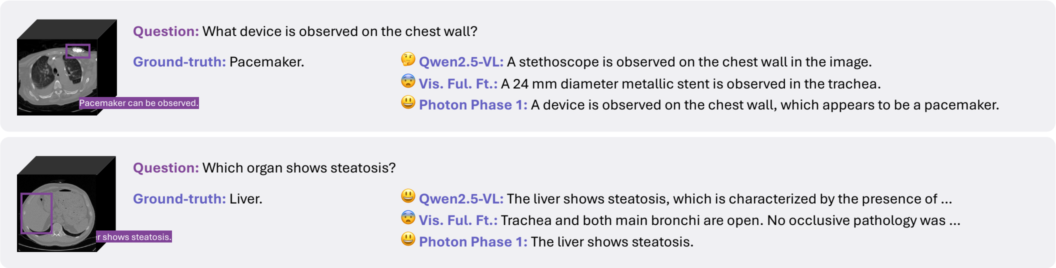

Question: What device is observed on the chest wall?

Ground-truth: Pacemaker.

🤔 **Qwen2.5-VL:** A stethoscope is observed on the chest wall in the image.
😨 **Vis. Ful. Ft.:** A 24 mm diameter metallic stent is observed in the trachea.
😃 **Photon Phase 1:** A device is observed on the chest wall, which appears to be a pacemaker.

Question: Which organ shows steatosis?

Ground-truth: Liver.

😃 **Qwen2.5-VL:** The liver shows steatosis, which is characterized by the presence of ...
😨 **Vis. Ful. Ft.:** Trachea and both main bronchi are open. No occlusive pathology was ...
😃 **Photon Phase 1:** The liver shows steatosis.

Figure 4: Visualization Results of base model and different visual alignment methods. Our method achieves alignment while avoiding mode collapse. Vis. Ful. Ft. = Visual Modules Fully Finetuned.

In the task-related finetuning stage, compared with other chosen layers, Photon achieves the best trade-off by placing the module at the $\ell = \ell_{n/4}$, attaining higher accuracy while maintaining efficiency. The importance of the core components is evident, removing ITS and SGP lowers static temporal diagnosis accuracy by more than 3%, increases the number of retained tokens, and slows training, confirming their necessity for both performance and efficiency. Regularization is also critical, since removing these terms not only reduces accuracy but also destabilizes training and undermines result reliability (Appendix A.2.3). Overall, Photon improves accuracy while substantially reducing computation. Compared with finetuned Qwen2.5-VL (Bai et al., 2025), it consistently achieves better performance while reducing inference memory usage by about two-thirds and achieving over a five-fold speedup. Gains in inference speed are more modest due to the use of KV Cache, but remain steady.

Beyond the main Photon design, we offer an alternative option called Photon Max. It reuses the original visual patch embedding layer of Qwen2.5-VL (Bai et al., 2025) with our components, improving existence detection and static temporal diagnosis by 2.4% and 4.9%, respectively, while training about 25% faster than Qwen2.5-VL with lower memory usage, thus serving as a more accuracy-oriented variant that remains more efficient than the original baseline.

5 Conclusion

We present Photon, an efficient MLLM framework for 3D medical volume understanding. Photon directly operates on 3D scans and integrates Instruction-conditioned Token Scheduling (ITS) with Surrogate Gradient Propagation (SGP) to achieve adaptive and consistent token reduction during both training and inference. ITS discretely selects informative tokens in the forward path and predicts adaptive sample-specific thresholds from instruction-vision interactions. SGP ensures effective gradient back-propagation in a discrete token dropping scenario. Through this innovative design, Photon reduces computational and memory costs while preserving clinically critical information. Experiments on various medical visual question answering benchmarks demonstrate that Photon achieves state-of-the-art performance with substantially fewer tokens and less computational overhead.

References

Saeed Ranjbar Alvar, Gursimran Singh, Mohammad Akbari, and Yong Zhang. Divprune: Diversity-based visual token pruning for large multimodal models. In *CVPR*, pp. 9392–9401, 2025. 3

Fan Bai, Yuxin Du, Tiejun Huang, Max Q-H Meng, and Bo Zhao. M3d: Advancing 3d medical image analysis with multi-modal large language models. *arXiv preprint arXiv:2404.00578*, 2024. 2, 3

Shuai Bai, Keqin Chen, Xuejing Liu, Jialin Wang, Wenbin Ge, Sibo Song, Kai Dang, Peng Wang, Shijie Wang, Jun Tang, et al. Qwen2. 5-vl technical report. *arXiv preprint arXiv:2502.13923*, 2025. 4, 9, 10, 16

Louis Blankemeier, Joseph Paul Cohen, Ashwin Kumar, Dave Van Veen, Syed Jamal Safdar Gardezi, Magdalini Paschali, Zhihong Chen, Jean-Benoit Delbrouck, Eduardo Reis, Cesar Truyts, et al. Merlin: A vision language foundation model for 3d computed tomography. *Research Square*, pp. rs–3, 2024. 2

Chubin Chen, Sujie Hu, Jiashu Zhu, Meiqi Wu, Jintao Chen, Yanxun Li, Nisha Huang, Chengyu Fang, Jiahong Wu, Xiangxiang Chu, et al. Taming preference mode collapse via directional decoupling alignment in diffusion reinforcement learning. *arXiv preprint arXiv:2512.24146*, 2025a. 24

Chubin Chen, Jiashu Zhu, Xiaokun Feng, et al. S^2-guidance: Stochastic self guidance for training-free enhancement of diffusion models. *arXiv preprint arXiv:2508.12880*, 2025b. 24

Junying Chen, Chi Gui, Ruyi Ouyang, Anningzhe Gao, Shunian Chen, Guiming Chen, Xidong Wang, Zhenyang Cai, Ke Ji, Xiang Wan, et al. Towards injecting medical visual knowledge into multimodal llms at scale. In *EMNLP*, pp. 7346–7370, 2024a. 2

Liang Chen, Haozhe Zhao, Tianyu Liu, Shuai Bai, Junyang Lin, Chang Zhou, and Baobao Chang. An image is worth 1/2 tokens after layer 2: Plug-and-play inference acceleration for large vision-language models. In *ECCV*, pp. 19–35. Springer, 2024b. 3

Yixiong Chen, Wenjie Xiao, Pedro RAS Bassi, Xinze Zhou, Sezgin Er, Ibrahim Ethem Hamamci, Zongwei Zhou, and Alan Yuille. Are vision language models ready for clinical diagnosis? a 3d medical benchmark for tumor-centric visual question answering. *arXiv preprint arXiv:2505.18915*, 2025c. 7, 18, 20, 21, 24

Tri Dao. FlashAttention-2: Faster attention with better parallelism and work partitioning. In *ICLR*, 2024. 17

Mohamed Dhouib, Davide Buscaldi, Sonia Vanier, and Aymen Shabou. Pact: Pruning and clustering-based token reduction for faster visual language models. In *CVPR*, pp. 14582–14592, 2025. 3

Chengyu Fang, Chunming He, Fengyang Xiao, Yulun Zhang, Longxiang Tang, Yuelin Zhang, Kai Li, and Xiu Li. Real-world image dehazing with coherence-based pseudo labeling and cooperative unfolding network. In *The Thirty-eighth Annual Conference on Neural Information Processing Systems*, 2024. 24

Chengyu Fang, Chunming He, Longxiang Tang, Yuelin Zhang, Chenyang Zhu, Yuqi Shen, Chubin Chen, Guoxia Xu, and Xiu Li. Integrating extra modality helps segmentor find camouflaged objects well. *arXiv preprint arXiv:2502.14471*, 2025. 24

Xiaotang Gai, Jiaxiang Liu, Yichen Li, Zijie Meng, Jian Wu, and Zuozhu Liu. 3d-rad: A comprehensive 3d radiology med-vqa dataset with multi-temporal analysis and diverse diagnostic tasks. *arXiv preprint arXiv:2506.11147*, 2025. 7, 18, 21, 23, 24

Ibrahim Ethem Hamamci, Sezgin Er, and Bjoern Menze. Ct2rep: Automated radiology report generation for 3d medical imaging. In *MICCAI*, pp. 476–486. Springer, 2024a. 2

Ibrahim Ethem Hamamci, Sezgin Er, Chenyu Wang, Furkan Almas, Ayse Gulnihan Simsek, Sevval Nil Esirgun, Irem Doga, Omer Faruk Durugol, Weicheng Dai, Murong Xu, et al. Developing generalist foundation models from a multimodal dataset for 3d computed tomography. *arXiv preprint arXiv:2403.17834*, 2024b. 2, 18, 24

Kai Han, Jianyuan Guo, Yehui Tang, Wei He, Enhua Wu, and Yunhe Wang. Free video-llm: Prompt-guided visual perception for efficient training-free video llms. *arXiv preprint arXiv:2410.10441*, 2024. 3

Chunming He, Rihan Zhang, Fengyang Xiao, Chenyu Fang, Longxiang Tang, and Yulun Zhang. Run: Reversible unfolding network for concealed object segmentation. *ICML*, 2025. 24

Kai Huang, Hao Zou, Ye Xi, BoChen Wang, Zhen Xie, and Liang Yu. Ivtp: Instruction-guided visual token pruning for large vision-language models. In *European Conference on Computer Vision*, pp. 214–230. Springer, 2024. 3

Songtao Jiang, Yuan Wang, Sibo Song, Yan Zhang, Zijie Meng, Bohan Lei, Jian Wu, Jimeng Sun, and Zuozhu Liu. Omniv-med: Scaling medical vision-language model for universal visual understanding. *arXiv preprint arXiv:2504.14692*, 2025. 3

Zheng Jiang, Heng Guo, Chengyu Fang, Changchen Xiao, Xinyang Hu, Lifeng Sun, and Minfeng Xu. Medvr: Annotation-free medical visual reasoning via agentic reinforcement learning. In *The Fourteenth International Conference on Learning Representations*, 2026. 24

Yuxiang Lai, Jike Zhong, Ming Li, Shitian Zhao, and Xiaofeng Yang. Med-r1: Reinforcement learning for generalizable medical reasoning in vision-language models. *arXiv preprint arXiv:2503.13939*, 2025. 2

Changsun Lee, Sangjoon Park, Cheong-Il Shin, Woo Hee Choi, Hyun Jeong Park, Jeong Eun Lee, and Jong Chul Ye. Read like a radiologist: Efficient vision-language model for 3d medical imaging interpretation. *arXiv preprint arXiv:2412.13558*, 2024. 2

Ao Li, Yuxiang Duan, Jinghui Zhang, Congbo Ma, Yutong Xie, Gustavo Carneiro, Mohammad Yaqub, and Hu Wang. Transprune: Token transition pruning for efficient large vision-language model. *arXiv preprint arXiv:2507.20630*, 2025a. 3

Chunyuan Li, Cliff Wong, Sheng Zhang, Naoto Usuyama, Haotian Liu, Jianwei Yang, Tristan Naumann, Hoifung Poon, and Jianfeng Gao. Llava-med: Training a large language-and-vision assistant for biomedicine in one day. In *NeurIPS*, volume 36, pp. 28541–28564, 2023a. 2

Junnan Li, Dongxu Li, Silvio Savarese, and Steven Hoi. Blip-2: Bootstrapping language-image pre-training with frozen image encoders and large language models. In *ICML*, pp. 19730–19742. PMLR, 2023b. 3

Wenxuan Li, Chongyu Qu, Xiaoxi Chen, Pedro RAS Bassi, Yijia Shi, Yuxiang Lai, Qian Yu, Huimin Xue, Yixiong Chen, Xiaorui Lin, et al. Abdomenatlas: A large-scale, detailed-annotated, & multi-center dataset for efficient transfer learning and open algorithmic benchmarking. *Medical Image Analysis*, 97:103285, 2024a. 18, 20, 24

Xingyuan Li, Yang Zou, Jinyuan Liu, Zhiying Jiang, Long Ma, Xin Fan, and Risheng Liu. From text to pixels: A context-aware semantic synergy solution for infrared and visible image fusion. *arXiv preprint arXiv:2401.00421*, 2023c. 24

Xingyuan Li, Zirui Wang, Yang Zou, Zhixin Chen, Jun Ma, Zhiying Jiang, Long Ma, and Jinyuan Liu. Difiisr: A diffusion model with gradient guidance for infrared image super-resolution. In *Proceedings of the Computer Vision and Pattern Recognition Conference*, pp. 7534–7544, 2025b. 24

Yanwei Li, Chengyao Wang, and Jiaya Jia. Llama-vid: An image is worth 2 tokens in large language models. In *ECCV*, pp. 323–340. Springer, 2024b. 3

Tianwei Lin, Wenqiao Zhang, Sijing Li, Yuqian Yuan, Binhe Yu, Haoyuan Li, Wanggui He, Hao Jiang, Mengze Li, Xiaohui Song, et al. Healthgpt: A medical large vision-language model for unifying comprehension and generation via heterogeneous knowledge adaptation. *arXiv preprint arXiv:2502.09838*, 2025a. 2

Yunlong Lin, Zixu Lin, Kunjie Lin, Jinbin Bai, Panwang Pan, Chenxin Li, Haoyu Chen, Zhongdao Wang, Xinghao Ding, Wenbo Li, et al. Jarvisart: Liberating human artistic creativity via an intelligent photo retouching agent. *arXiv preprint arXiv:2506.17612*, 2025b. 24

Yunlong Lin, Linqing Wang, Kunjie Lin, Zixu Lin, Kaixiong Gong, Wenbo Li, Bin Lin, Zhenxi Li, Shiyi Zhang, Yuyang Peng, et al. Jarvisevo: Towards a self-evolving photo editing agent with synergistic editor-evaluator optimization. *arXiv preprint arXiv:2511.23002*, 2025c. 24

Bo Liu, Li-Ming Zhan, Li Xu, Lin Ma, Yan Yang, and Xiao-Ming Wu. Slake: A semantically-labeled knowledge-enhanced dataset for medical visual question answering. In *2021 IEEE 18th international symposium on biomedical imaging (ISBI)*, pp. 1650–1654. IEEE, 2021. 18, 21

Che Liu, Zheng Jiang, Chengyu Fang, Heng Guo, Yan-Jie Zhou, Jiaqi Qu, Le Lu, and Minfeng Xu. M3ret: Unleashing zero-shot multimodal medical image retrieval via self-supervision. *arXiv preprint arXiv:2509.01360*, 2025a. 24

Jizhihui Liu, Feiyi Du, Guangdao Zhu, Niu Lian, Jun Li, and Bin Chen. Hiprune: Training-free visual token pruning via hierarchical attention in vision-language models. *arXiv preprint arXiv:2508.00553*, 2025b. 8

Tianyi Liu, Haochuan Jiang, and Kaizhu Huang. Kmd: Koopman multi-modality decomposition for generalized brain tumor segmentation under incomplete modalities. In *Proceedings of the Computer Vision and Pattern Recognition Conference*, pp. 15663–15671, 2025c. 24

Tianyi Liu, Zhaorui Tan, Muyin Chen, Xi Yang, Haochuan Jiang, and Kaizhu Huang. Medmap: Promoting incomplete multi-modal brain tumor segmentation with alignment. *IEEE Journal of Biomedical and Health Informatics*, 2025d. 24

Yizhen Luo, Jiahuan Zhang, Siqi Fan, Kai Yang, Yushuai Wu, Mu Qiao, and Zaiqing Nie. Biomedgpt: Open multimodal generative pre-trained transformer for biomedicine. *arXiv preprint arXiv:2308.09442*, 2023. 2

Yue Ma, Zexuan Yan, Hongyu Liu, Hongfa Wang, Heng Pan, Yingqing He, Junkun Yuan, Ailing Zeng, Chengfei Cai, Heung-Yeung Shum, et al. Follow-your-emoji-faster: Towards efficient, fine-controllable, and expressive freestyle portrait animation. *arXiv preprint arXiv:2509.16630*, 2025. 24

Pavlo Molchanov, Stephen Tyree, Tero Karras, Timo Aila, and Jan Kautz. Pruning convolutional neural networks for resource efficient inference. *arXiv preprint arXiv:1611.06440*, 2016. 17

Jiazhen Pan, Che Liu, Junde Wu, Fenglin Liu, Jiayuan Zhu, Hongwei Bran Li, Chen Chen, Cheng Ouyang, and Daniel Rueckert. Medvlm-r1: Incentivizing medical reasoning capability of vision-language models (vlms) via reinforcement learning. In *MICCAI*, 2025. 2

Jeff Rasley, Samyam Rajbhandari, Olatunji Ruwase, and Yuxiong He. Deepspeed: System optimizations enable training deep learning models with over 100 billion parameters. In *Proceedings of the 26th ACM SIGKDD international conference on knowledge discovery & data mining*, pp. 3505–3506, 2020. 17

Andrew Sellergren, Sahar Kazemzadeh, Tiam Jaroensri, Atilla Kiraly, Madeleine Traverse, Timo Kohlberger, Shawn Xu, Fayaz Jamil, Cían Hughes, Charles Lau, et al. Medgemma technical report. *arXiv preprint arXiv:2507.05201*, 2025. 2

Yuzhang Shang, Mu Cai, Bingxin Xu, Yong Jae Lee, and Yan Yan. Llava-prumerge: Adaptive token reduction for efficient large multimodal models. *arXiv preprint arXiv:2403.15388*, 2024. 2, 3

Boyuan Sun, Jiaxing Zhao, Xihan Wei, and Qibin Hou. Llava-scissor: Token compression with semantic connected components for video llms. *arXiv preprint arXiv:2506.21862*, 2025. 3

Guankun Wang, Long Bai, Junyi Wang, Kun Yuan, Zhen Li, Tianxu Jiang, Xiting He, Jinlin Wu, Zhen Chen, Zhen Lei, et al. Endochat: Grounded multimodal large language model for endoscopic surgery. *Medical Image Analysis*, pp. 103789, 2025a. 24

Guankun Wang, Han Xiao, Renrui Zhang, Huxin Gao, Long Bai, Xiaoxiao Yang, Zhen Li, Hongsheng Li, and Hongliang Ren. Copesd: A multi-level surgical motion dataset for training large vision-language models to co-pilot endoscopic submucosal dissection. In *Proceedings of the 33rd ACM International Conference on Multimedia*, pp. 12636–12643, 2025b. 24

Hongqiu Wang, Guang Yang, Shichen Zhang, Jing Qin, Yike Guo, Bo Xu, Yueming Jin, and Lei Zhu. Video-instrument synergistic network for referring video instrument segmentation in robotic surgery. *IEEE Transactions on Medical Imaging*, 2024a. 24

Hongqiu Wang, Wu Chen, Xiangde Luo, Zhaohu Xing, Lihao Liu, Jing Qin, Shaozhi Wu, and Lei Zhu. Toward fair and accurate cross-domain medical image segmentation: A vlm-driven active domain adaptation paradigm. In *Proceedings of the IEEE/CVF International Conference on Computer Vision*, pp. 24102–24112, 2025c. 24

Jiangshan Wang, Zeqiang Lai, Jiarui Chen, Jiayi Guo, Hang Guo, Xiu Li, Xiangyu Yue, and Chunchao Guo. Elastic diffusion transformer. *arXiv preprint arXiv:2602.13993*, 2026a. 24

Jiangshan Wang, Kang Zhao, Jiayi Guo, Jiayu Wang, Hang Guo, Chenyang Zhu, Xiangyu Yue, and Xiu Li. Precisecache: Precise feature caching for efficient and high-fidelity video generation. In *The Fourteenth International Conference on Learning Representations*, 2026b. 24

Xiao Wang, Qingyi Si, Jianlong Wu, Shiyu Zhu, Li Cao, and Liqiang Nie. Retake: Reducing temporal and knowledge redundancy for long video understanding. *arXiv preprint arXiv:2412.20504*, 2024b. 3

Chaoyi Wu, Xiaoman Zhang, Ya Zhang, Yanfeng Wang, and Weidi Xie. Towards generalist foundation model for radiology by leveraging web-scale 2d&3d medical data. *arXiv preprint arXiv:2308.02463*, 2023. 2, 3

Junbin Xiao, Xindi Shang, Angela Yao, and Tat-Seng Chua. Next-qa: Next phase of question-answering to explaining temporal actions. In *Proceedings of the IEEE/CVF conference on computer vision and pattern recognition*, pp. 9777–9786, 2021. 18, 22

Long Xing, Qidong Huang, Xiaoyi Dong, Jiajie Lu, Pan Zhang, Yuhang Zang, Yuhang Cao, Conghui He, Jiaqi Wang, Feng Wu, et al. Pyramiddrop: Accelerating your large vision-language models via pyramid visual redundancy reduction. *arXiv preprint arXiv:2410.17247*, 2024. 3

Weiwen Xu, Hou Pong Chan, Long Li, Mahani Aljunied, Ruifeng Yuan, Jianyu Wang, Chenghao Xiao, Guizhen Chen, Chaoqun Liu, Zhaodonghui Li, et al. Lingshu: A generalist foundation model for unified multimodal medical understanding and reasoning. *arXiv preprint arXiv:2506.07044*, 2025. 2

An Yang, Anfeng Li, Baosong Yang, Beichen Zhang, Binyuan Hui, Bo Zheng, Bowen Yu, Chang Gao, Chengen Huang, Chenxu Lv, et al. Qwen3 technical report. *arXiv preprint arXiv:2505.09388*, 2025a. 21

Cheng Yang, Yang Sui, Jinqi Xiao, Lingyi Huang, Yu Gong, Chendi Li, Jinghua Yan, Yu Bai, Ponnuswamy Sadayappan, Xia Hu, et al. Topv: Compatible token pruning with inference time optimization for fast and low-memory multimodal vision language model. In *CVPR*, pp. 19803–19813, 2025b. 3

Jihan Yang, Shusheng Yang, Anjali W Gupta, Rilyn Han, Li Fei-Fei, and Saining Xie. Thinking in space: How multimodal large language models see, remember, and recall spaces. In *CVPR*, pp. 10632–10643, 2025c. 18

Senqiao Yang, Yukang Chen, Zhuotao Tian, Chengyao Wang, Jingyao Li, Bei Yu, and Jiaya Jia. Visionzip: Longer is better but not necessary in vision language models. In *CVPR*, pp. 19792–19802, 2025d. 2, 3, 8

Linli Yao, Lei Li, Shuhuai Ren, Lean Wang, Yuanxin Liu, Xu Sun, and Lu Hou. Deco: Decoupling token compression from semantic abstraction in multimodal large language models. *arXiv preprint arXiv:2405.20985*, 2024. 3

Xubing Ye, Yukang Gan, Yixiao Ge, Xiao-Ping Zhang, and Yansong Tang. Atp-llava: Adaptive token pruning for large vision language models. In *CVPR*, pp. 24972–24982, 2025. 2, 3

Suhao Yu, Haojin Wang, Juncheng Wu, Cihang Xie, and Yuyin Zhou. Medframeqa: A multi-image medical vqa benchmark for clinical reasoning. *arXiv preprint arXiv:2505.16964*, 2025. 18, 20, 21

Ce Zhang, Kaixin Ma, Tianqing Fang, Wenhao Yu, Hongming Zhang, Zhisong Zhang, Yaqi Xie, Katia Sycara, Haitao Mi, and Dong Yu. Vscan: Rethinking visual token reduction for efficient large vision-language models. *arXiv preprint arXiv:2505.22654*, 2025a. 3

Jiajun Zhang, Jianke Zhang, Zeyu Cui, Jiaxi Yang, Lei Zhang, Binyuan Hui, Qiang Liu, Zilei Wang, Liang Wang, and Junyang Lin. Plotcraft: Pushing the limits of llms for complex and interactive data visualization. *arXiv preprint arXiv:2511.00010*, 2025b. 24

Qizhe Zhang, Aosong Cheng, Ming Lu, Renrui Zhang, Zhiyong Zhuo, Jiajun Cao, Shaobo Guo, Qi She, and Shanghang Zhang. Beyond text-visual attention: Exploiting visual cues for effective token pruning in vlms. *arXiv preprint arXiv:2412.01818*, 2025c. 3

Qizhe Zhang, Mengzhen Liu, Lichen Li, Ming Lu, Yuan Zhang, Junwen Pan, Qi She, and Shanghang Zhang. Beyond attention or similarity: Maximizing conditional diversity for token pruning in mllms. *arXiv preprint arXiv:2506.10967*, 2025d. 3

A Appendix

A.1 Methodology

A.1.1 Training Process

Unlike most previous 3D medical MLLM methods that use a three-stage pipeline (including vision pretraining, vision language alignment, and vision language instruction finetuning), we design a lighter and more efficient two-stage training strategy.

In Phase 1, we perform visual embedding alignment by training the 3D vision patch embedding layer of the visual encoder on volume-radiology report data with a learning rate of $1e^{-4}$ under annealing. The ViT backbone retains its pretrained weights from Qwen2.5-VL (Bai et al., 2025), and both the backbone and the MLP aligner are kept frozen to preserve the priors learned from large-scale natural images. The Qwen2.5-VL decoder is also frozen and serves only as the alignment target. We find that fully finetuning the vision encoder tends to cause overfitting and negatively affects the decoder's ability to follow instructions and interpret visual inputs. By updating only the 3D vision patch embedding layer, this stage improves efficiency, maintains generalization, and avoids the need to re-pretrain the visual encoder or re-align vision and language on large-scale medical data.

In Phase 2, based on the alignment obtained in Phase 1, we replace the Qwen2.5-VL language decoder with the Photon language decoder that integrates our ITS and SGP modules, while retaining the backbone parameters reused from Qwen2.5-VL. This design allows us to directly inherit the alignment results and the pretrained capabilities of Qwen2.5-VL without restarting pretraining from scratch. In this stage, we unfreeze all modules and finetune them on the task-specific training set for optimization with a learning rate of $1e^{-5}$ under a cosine annealing schedule.

A.1.2 Details of threshold feature construction and pruning

We detail the three feature blocks and the subsequent thresholding and selection.

Normalization for ranking. Given raw logits $d = \{d_j\}_{j \in \mathcal{V}^{(b)}}$, we define the min-max normalized saliency scores:

$$\rho_j = \frac{d_j - \min_{k \in \mathcal{V}^{(b)}} d_k}{\max_{k \in \mathcal{V}^{(b)}} d_k - \min_{k \in \mathcal{V}^{(b)}} d_k + \epsilon}, \qquad j \in \mathcal{V}^{(b)}.$$

This rescales logits to $[0, 1]$ and preserves within-sample ordering.

Block 1: shape descriptor from normalized scores. From $\rho = \{\rho_j\}$ we compute:

$$\Psi(\rho) = \big[\mu(\rho),\ \mathrm{Std}(\rho),\ \min(\rho),\ \max(\rho),\ Q_{1/4}(\rho),\ \mathrm{med}(\rho)\big] \in \mathbb{R}^6,$$

capturing central tendency, spread, range, lower quartile, and median in a scale-free manner.

Block 2: scale descriptor from raw logits. From d we extract absolute-scale statistics:

$$\Phi(d) = \big[\mu(d),\ \mathrm{Std}(d),\ \min(d),\ \max(d)\big] \in \mathbb{R}^4,$$

which retain level and variability on the original linear scale.

Block 3: compressed descriptor from signed log view. To summarize large magnitudes while preserving sign, we use:

$$\mathrm{slog}(x) = \mathrm{sign}(x)\ \log\big(1 + |x|\big),$$

and define:

$$\Upsilon(\mathrm{slog}(d)) = \big[\mu(\mathrm{slog}(d)),\ \max(\mathrm{slog}(d))\big] \in \mathbb{R}^2.$$

This provides compressed indicators of overall level and dominant peaks.

A.1.3 Gradient dynamics of the surrogate

We provide a formal analysis of the surrogate gradient mechanism described in the main text. The token-level retention probability is defined as:

$$q = \sigma\left(\tfrac{\rho - \theta}{\tau_{\mathrm{ce}}}\right),$$

where ρ denotes the normalized saliency score and θ is the instance-specific threshold predicted by ITP. The surrogate gradient with respect to q takes the form:

$$\frac{\partial \mathcal{L}}{\partial q} = \beta\, d\, s\, \max\{q(1-q),\, \epsilon_{sat}\}, \qquad d = 0.5 - \mathrm{sg}(r), \quad r = \psi(z),\ \psi(0) = 0.5,$$

where d is the directional term measuring deviation from the neutral point 0.5, s is the magnitude factor obtained from activation-gradient interactions, β is a balancing coefficient, and the saturation term $\max\{q(1-q),\, \epsilon_{sat}\}$ prevents vanishing gradients near the extremes. As in the main text, all updates are restricted to visual positions, so that only active tokens contribute.

The partial derivatives of q are:

$$\frac{\partial q}{\partial \theta} = -\tfrac{1}{\tau_{\text{ce}}}\, \sigma'\!\left(\tfrac{\rho-\theta}{\tau_{\text{ce}}}\right) < 0, \qquad \frac{\partial q}{\partial \rho} = \tfrac{1}{\tau_{\text{ce}}}\, \sigma'\!\left(\tfrac{\rho-\theta}{\tau_{\text{ce}}}\right) > 0,$$

which leads to:

$$\frac{\partial \mathcal{L}}{\partial \theta} = \frac{\partial \mathcal{L}}{\partial q} \cdot \frac{\partial q}{\partial \theta}, \qquad \frac{\partial \mathcal{L}}{\partial \rho} = \frac{\partial \mathcal{L}}{\partial q} \cdot \frac{\partial q}{\partial \rho}.$$

When the directional term satisfies $d < 0$, we obtain $\frac{\partial \mathcal{L}}{\partial q} < 0$. Consequently, $\frac{\partial \mathcal{L}}{\partial \theta} > 0$ and $\frac{\partial \mathcal{L}}{\partial \rho} < 0$, so gradient descent decreases θ and increases ρ. This enlarges the margin $\rho - \theta$, raises q, and thereby promotes token retention.

Conversely, when $d > 0$, we obtain $\frac{\partial \mathcal{L}}{\partial q} > 0$. In this case, $\frac{\partial \mathcal{L}}{\partial \theta} < 0$ and $\frac{\partial \mathcal{L}}{\partial \rho} > 0$, so gradient descent increases θ and decreases ρ. This reduces the margin $\rho - \theta$, lowers q, and thereby increases the tendency toward pruning.

Overall, the surrogate gradient dynamics remain consistent with the intended behavior: tokens assessed as informative are reinforced toward retention, while less informative tokens receive weaker gradients and are progressively pruned.

A.1.4 Derivation of token importance via first-order approximation

Let $\mathrm{T}_{\text{vis}}^{\ell} \in \mathbb{R}^{L \times d}$ denote the visual hidden states at decoder layer ℓ. Removing token j is modeled as setting its hidden state $(\mathrm{T}_{\text{vis}}^{\ell})_j$ to zero while keeping all other tokens unchanged. Applying a first-order Taylor expansion of the training loss $\mathcal{L}$ around $\mathrm{T}_{\text{vis}}^{\ell}$ gives

$$\mathcal{L}(\mathrm{T}_{\text{vis}}^{\ell} - (\mathrm{T}_{\text{vis}}^{\ell})_j) \;\approx\; \mathcal{L}(\mathrm{T}_{\text{vis}}^{\ell}) - \left\langle (\mathrm{T}_{\text{vis}}^{\ell})_j,\; \left(\tfrac{\partial \mathcal{L}}{\partial \mathrm{T}_{\text{vis}}^{\ell}}\right)_j \right\rangle,$$

so that the predicted loss variation caused by discarding token j is

$$\Delta \mathcal{L}_j \;\approx\; -\left\langle (\mathrm{T}_{\text{vis}}^{\ell})_j,\; \left(\tfrac{\partial \mathcal{L}}{\partial \mathrm{T}_{\text{vis}}^{\ell}}\right)_j \right\rangle.$$

This matches the Taylor-based importance criterion proposed for filter and neuron pruning (Molchanov et al., 2016). We therefore adopt the activation-gradient product as a token-level importance signal and define

$$\eta_j \;=\; \left\langle (\mathrm{T}_{\text{vis}}^{\ell})_j,\; \left(\tfrac{\partial \mathcal{L}}{\partial \mathrm{T}_{\text{vis}}^{\ell}}\right)_j \right\rangle,$$

This extends the classical Taylor criterion to multimodal token reduction with differentiable masking, and the resulting scores are standardized and clipped across active tokens for stable optimization.

A.2 Experiments

A.2.1 Experimental Setup

In our experiments, training was performed on 16 NVIDIA H20 GPUs with BF16 precision with Deepspeed ZeRO2 (Rasley et al., 2020), and inference was conducted on 8 NVIDIA H20 GPUs. We set $\tau_{\text{ce}} = 0.2$ and configured SGP with $\epsilon_{\text{std}} = 3 \times 10^{-3}$, $(s_{\min}, s_{\max}) = (0.5, 2.0)$, $\beta = 0.8$, $\epsilon_{sat} = 5 \times 10^{-3}$, r_{min} and r_{max} are set to 0.3 and 0.8 respectively. Unless otherwise noted, ITS and SGP are applied at $\ell = \ell_{n/4}$. Optimization uses AdamW, and FlashAttention2 (Dao, 2024) is enabled in all attention layers.

A.2.2 Tasks, Datasets and Metrics

In Phase 1 of training, the visual embedding alignment process was trained on the volume-caption pairs of CT-RATE (we use 47,141 out of 50,188 pairs, reconstructed from 25,692 volumes belonging to 21,304 patients for training) (Hamamci et al., 2024b), AbdomenAtlas 3.0 (we use 8,334 out of 9,262 pairs for training) (Li et al., 2024a), and our internal dataset (we use 27,577 pairs for training). To address the potential overlap of identical volumes between Phase 1 and Phase 2, we adopt the Phase 2 data partitioning scheme in Phase 1, thereby preventing data leakage.

In Phase 2 of training, we finetune all model parameters using task-specific data. We employ two large-scale 3D CT VQA benchmarks: 3D-RAD (Gai et al., 2025) and DeepTumorVQA (Chen et al., 2025c), which together span descriptive, recognition, and reasoning-oriented diagnostic scenarios under clinically relevant protocols. We elaborate on these two datasets as follows.

3D-RAD (Gai et al., 2025) is a large-scale 3D medical VQA benchmark built upon CT-RATE (Hamamci et al., 2024b), comprising 16,188 CT scans from 11,255 patients with strict train-test separation. It covers six tasks (anomaly detection, image observation, medical measurement, existence detection, static temporal diagnosis, and longitudinal temporal diagnosis), supporting both open- and closed-ended questions. QA pairs are generated from radiology reports and multi-label annotations using task-specific templates, and refined through an LLM with human verification pipeline with over 91% factual alignment. The final dataset provides 33,910 curated benchmark QA pairs and 136,195 training pairs, enabling comprehensive evaluation of multi-task and multi-temporal reasoning in clinically realistic settings.

DeepTumorVQA (Chen et al., 2025c) is built from 9,262 abdominal CT volumes. The benchmark provides 355,962 training and 39,650 testing QA pairs across measurement, recognition, visual reasoning, and medical reasoning categories, covering both multiple-choice and free-text formats. Evaluation follows task-specific protocols, including accuracy for multiple-choice, exact match for free-text answers, mean relative accuracy (MRA) (Yang et al., 2025c) for numerical prediction, and CE for region-level clinical correctness. This design ensures reliable assessment of both reasoning capability and clinical validity.

SLAKE (Liu et al., 2021) is a large-scale bilingual medical visual question-answering benchmark that features richly annotated radiology images and knowledge graph support. The dataset covers multiple imaging modalities and several body regions. QA pairs span question types such as imaging plane, modality, organ detection, abnormalities, and knowledge-graph reasoning. The benchmark supports both closed-ended and open-ended question formats and is designed for evaluating visual reasoning plus medical knowledge reasoning in a multilingual setting.

NExT-QA (Xiao et al., 2021) is a video question answering benchmark designed to move beyond scene description toward explaining causal and temporal action relations. It contains 5,440 real-world videos and 52,044 human-annotated QA pairs, organized into three categories: causal questions that require identifying visible cause–effect relations, temporal questions that probe ordering of actions, and descriptive questions covering objects, attributes and events.

MedFrameQA (Yu et al., 2025) is a benchmark designed for multi-image medical visual question answering that reflects more realistic clinical workflows. MedFrameQA contains 2,851 clinically grounded VQA items constructed from 9,237 high-quality frames extracted from 3,420 instructional medical videos. Each question is paired with two to five temporally coherent frames that share a continuous diagnostic focus. The dataset spans nine human body systems and 43 organs across diverse imaging modalities, forming a challenging setting that requires models to integrate complementary evidence across multiple images rather than relying on single-frame cues.

We evaluate model performance using a combination of text generation and classification metrics. For free-text tasks, we adopt BLEU, ROUGE, and BERT Score to assess fluency, lexical overlap, and semantic similarity between generated and reference answers. BLEU captures n-gram precision, ROUGE emphasizes recall-oriented overlap, and BERT Score leverages contextual embeddings for semantic alignment. For categorical predictions such as existence detection and temporal diagnosis, Accuracy is reported. For numerical free-text answers, we further apply the Mean Relative Accuracy (MRA) (Yang et al., 2025c) metric, which measures correctness under a range of relative error thresholds, reflecting clinical tolerance in quantitative assessment. Together, these metrics provide a comprehensive evaluation across descriptive, reasoning, and measurement-oriented tasks.

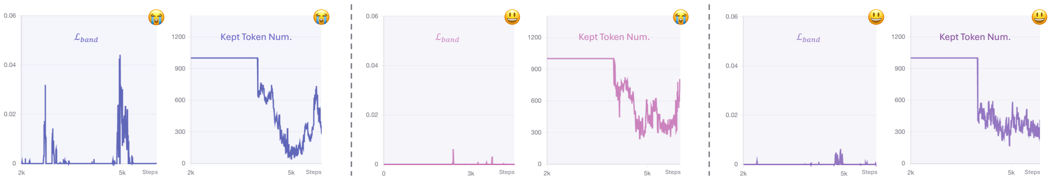

Figure 5: Visualization of retention band triggers (Eq. (18)) and the number of kept tokens. Left: training without robust regularization, middle: training without flip regularization, right: training with both regularizations. A lower activation frequency and smaller magnitude of the retention band indicate more stable pruning during training.

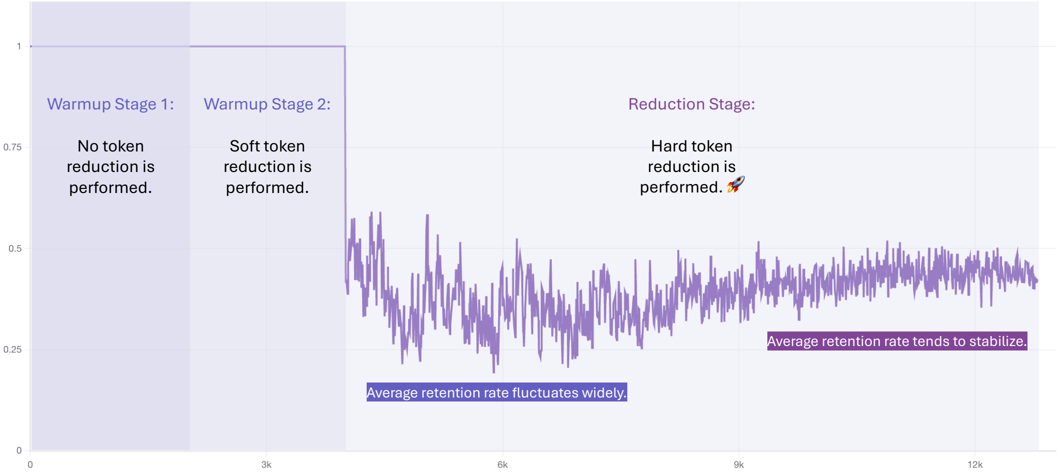

Figure 6: Visualization of retention rate of training time. Our token reduction method exhibits an average retention rate that fluctuates within a reasonable range before steadily stabilizing, indicating convergence toward an appropriate per-sample threshold estimation.

A.2.3 Analysis of Soft Retention Band and Regularization

The soft retention band is designed as a safeguard mechanism rather than a regular penalty. Under normal conditions, it has little impact on performance because most retention probabilities lie within the expected range and are not penalized. Its main role emerges in extreme situations, where the predictor deviates sharply from a reasonable retention ratio. In such cases, the band introduces corrective pressure that pulls the retention ratio back into a stable range, preventing collapse.

Fig. 5 compares the trigger visualization of the soft retention band and the number of kept tokens under different regularization settings. The instability mainly arises from the limited visual priors of the pretrained backbone in 3D medical domains. Without sufficient prior knowledge, the predictor struggles to identify clinically relevant regions and systematically underestimates the importance of visual tokens. As shown in the left plots, in the absence of the robust regularizer this bias is amplified: the predictor tends to discard visual tokens, leading to unstable and sometimes extreme fluctuations in the retention ratio that reflect insufficient grounding in image evidence. The middle plots show that when only the robust term is applied but the flip regularizer is removed, pruning becomes smoother but the model starts to overfit spurious retention patterns, which undermines stability. By contrast, the right plots demonstrate that using both regularizers produces stable retention dynamics: the robust term suppresses neglect of visual content and constrains excessive pruning, while the flip term prevents shortcut reliance on fixed masks. Together, they enforce a balanced reliance on both visual and textual signals, resulting in smoother training and stronger visual grounding.

A.2.4 Token Reduction Analysis

Fig. 6 illustrates the progression of the average token retention rate during training Phase 2. In Warmup Stage 1, no reduction is applied and the rate remains fixed at 1.0. In Warmup Stage 2, the retention rate also stays at 1.0, but soft masking is applied to tokens so that the predictor begins learning threshold estimation, providing a gradual transition between full retention and hard pruning.

Table 5: Clinical Metrics of Kidney tumor recognition (sensitivity, specificity, and accuracy (%)).

Metric	RadFM	M3D-P3	M3D-L2	Merlin	CT-CHAT	Photon	Photon Bootstrap
Sensitivity	75.2	0.0	0.0	50.2	0.0	81.2± 1.7	81.7 [78.6, 84.7]
Specificity	98.6	100.0	100.0	51.2	100.0	95.2± 0.1	95.3 [93.8, 96.6]
Accuracy	88.6	57.4	57.4	50.7	57.4	89.3± 0.7	89.5 [87.9, 91.1]

Table 6: Photon performance on the AbdomenAtlas3.0-style OOD split of DeepTumorVQA. Results are reported for multi-choice and free-text variants (accuracy (%)).

Method	Avg. keep tok.	Meas.	Recog.	Vis. Rsn.	Med. Rsn.	Overall
Photon OOD Multi-Choice	0.34K	0.745	0.599	0.636	0.677	0.648
Photon OOD Free-Text	0.40K	0.459	0.643	0.520	0.599	0.570

Once entering the Reduction Stage, hard pruning is applied: the retention rate first oscillates as the predictor adapts and then gradually stabilizes. This staged schedule prevents premature pruning and enables a smooth shift from probability learning to discrete token removal.

A.2.5 Analysis in Clinical Metrics

As noted in (Chen et al., 2025c), lesion recognition poses greater challenges for MLLMs than general VQA tasks, since reliable clinical application requires balanced sensitivity, specificity, and accuracy. Table 5 highlights the diversity of model behaviors: some approaches emphasize specificity at the expense of detection, while others show higher sensitivity but limited overall stability. These differences reflect the difficulty of consistently capturing subtle lesion signals in raw 3D volumes without explicit spatial supervision.

To account for randomness, we repeat the experiment with ten independent seeds on under the same protocol. We report mean $\pm$ standard deviation for all medical metrics. Photon exceeds the strongest baseline under every seed, which indicates that the improvements are stable with respect to initialization. For the main Photon results, we also estimate test-set uncertainty with 1000 bootstrap resamples of evaluation questions and report 95 percent confidence intervals. The intervals remain narrow, showing that the observed gains are not due to sampling noise.

In addition, Photon achieves a more stable balance across the three metrics. It maintains competitive accuracy while improving lesion detection rates, thereby reducing the likelihood of missed cases without compromising overall reliability. This balance across sensitivity, specificity, and accuracy suggests that Photon better aligns with clinical requirements compared with prior MLLM baselines.

A.2.6 Zero-shot and out-of-domain evaluation

In this section we study whether Photon maintains robustness and efficiency when evaluated outside its training distribution. Here we focus on two complementary scenarios: (1) institution-level out-of-domain (OOD) evaluation on DeepTumorVQA (Chen et al., 2025c) using the AbdomenAtlas3.0-based (Li et al., 2024a) split, and (2) a fully training-free zero-shot setting on MedFrameQA (Yu et al., 2025).

Institution-level OOD split on DeepTumorVQA. To evaluate robustness under distribution shift, we follow the AbdomenAtlas3.0 OOD split and redivide DeepTumorVQA into training and test sets based on medical institutions, which also induces changes in population, devices, and imaging protocols. We report results on free-text and multi-choice variants. Table 6 summarizes task-wise performance and the average number of retained vision tokens per sample.

Compared with the in-domain results reported in Table 2, the OOD setting leads to a moderate drop of approximately 0.038 and 0.049, respectively. This indicates that Photon preserves most of its accuracy under institution-level distribution shift while still retaining only $0.34\text{K} \sim 0.40\text{K}$ visual tokens on average, which confirms that the pruning mechanism does not destabilize cross-domain generalization.

Training-free zero-shot setting on MedFrameQA. To further isolate the effect of pruning and threshold estimation, we evaluate a training-free variant of Photon where the token scheduling module

Table 7: Zero-shot results on full MedFrameQA dataset. No additional medical fine-tuning is performed (accuracy (%)).

Method	Avg. keep tok.	CT	MRI	X-ray	Other	Ultrasound	Overall
Qwen2.5-VL 3B Zero-Shot	7.00K	0.461	0.460	0.485	0.477	0.432	0.460
Qwen2.5-VL 3B + ITS Zero-Shot	3.28K	0.459	0.456	0.488	0.470	0.426	0.457

is attached to Qwen2.5-VL 3B without any additional medical fine-tuning. We test this configuration in a strict zero-shot setting on MedFrameQA and compare it with the plain Qwen2.5-VL 3B backbone. Results across modalities and the average token keep rate are shown in Table 7.

The training-free Photon variant reduces the average token keep rate from $7.00K$ to $3.28K$ while maintaining almost identical zero-shot accuracy. Since the token scheduling module is attached as a plug-in and operates independently from the MLLM backbone parameters, these results indicate that the pruning and threshold estimation strategy preserves the backbone's zero-shot and generalization ability, even when no task-specific fine-tuning is applied.

A.2.7 More Ablation Study

Hyperparameters affecting pruning. We test the three hyperparameters that most directly control pruning behavior: the temperature τ_{ce}, the surrogate gradient weight β, and the saturation threshold ϵ_{sat}. As summarized in Table 8, changing these values mainly adjusts the average number of retained tokens, while task accuracy on all three 3D-RAD subtasks and the generative metrics remains stable. This supports the claim that our default configuration is already in a robust regime and that aggressive hyperparameter tuning is unnecessary in practice.

Robustness to noisy thresholds. To probe the robustness of the threshold predictor, we perturb the predicted thresholds at inference time with random multiplicative noise in $[-10\%, +10\%]$. The noisy variant in Table 8 shows only mild performance degradation, indicating that Photon does not rely on finely tuned thresholds and is tolerant to moderate estimation errors.

Scaling across backbones. Finally, we examine cross-model scaling. On Qwen2.5-VL, extending Photon from a 3B to a 7B backbone improves performance across tasks with similar retention ratios, and attaching Photon to Qwen3-VL (Yang et al., 2025a) 2B yields consistent pruning behavior without training collapse. Together, these results show that Photon is stable under hyperparameter changes, robust to noisy thresholds, and transferable across different backbone sizes and architectures.

A.3 Extend Photon to More Modalities

Instruction-conditioned scheduling across modalities. Instruction-conditioned Token Scheduling (ITS) does not operate on raw intensities or fixed spatial coordinates. Instead, it predicts a retention ratio from a normalized alignment distribution produced by the instruction-visual cross-attention. This distribution is normalized within each sample and depends on the relative ordering of token importance, rather than absolute intensities or fixed noise patterns. Therefore, ITS can adapt to changes in imaging centers, scanning protocols, slice numbers, orientations, spacing, and noise levels.

Results on MedFrameQA (Yu et al., 2025) and SLAKE (Liu et al., 2021). To test this property, we apply Photon to MedFrameQA, which contains diverse modalities and variable frame counts, slice numbers, and resolutions from multiple sources. We randomly split MedFrameQA (Yu et al., 2025) into training and testing sets with a $9:1$ ratio, and compare the Qwen2.5-VL 3B backbone with and without Photon. As shown in Table 9, Photon reduces the average token keep rate from 1.0 to about 0.43 while slightly improving the overall accuracy, with consistent gains on CT, MRI, and X-ray and no degradation on ultrasound. This suggests that the same ITS configuration that works for 3D-RAD (Gai et al., 2025) and DeepTumorVQA (Chen et al., 2025c) also remains stable on a heterogeneous multimodal benchmark, supporting the view that ITS learns a task-guided token importance structure instead of a dataset-specific mask pattern.

We also study transfer to MRI data using the SLAKE (Liu et al., 2021) dataset. Here we focus on MRI-based VQA in SLAKE (Liu et al., 2021) and again compare the non-pruned Qwen2.5-VL 3B baseline with our pruned variant. Photon cuts the average keep rate to about 0.38 while keeping

Table 8: Ablation on key hyperparameters and robustness of Photon. τ_{ce} controls the temperature for contrastive estimation; β balances surrogate gradient strength; ϵ_{sat} defines the saturation suppression threshold. The last block tests robustness under noisy threshold perturbation and cross-model scaling.

Setting	**E.D.**	**S.T.D.**	**L.T.D.**	**Medical Measurement**			**Image Observation**			**Anomaly Detection**			**Avg. Train Tok.**
	Acc.	Acc.	Acc.	BLEU	ROUGE	BERT	BLEU	ROUGE	BERT	BLEU	ROUGE	BERT	
Effect of τ_{ce} (temperature for contrastive estimation).													
τ_{ce}=0.10	82.44	51.66	77.66	38.65	39.87	96.20	51.11	56.77	93.61	41.95	46.91	91.86	0.42K
τ_{ce}=0.20	83.07	52.86	77.01	37.74	39.36	96.14	51.59	56.66	93.62	42.33	47.50	91.96	0.39K
τ_{ce}=0.50	82.88	52.13	77.71	38.59	39.77	96.25	51.61	56.16	93.53	41.73	46.81	91.87	0.32K
Effect of β (surrogate gradient weight).													
β=0.5	82.99	52.25	75.57	37.05	38.45	96.04	51.60	56.12	93.64	41.76	47.18	91.90	0.46K
β=0.8	83.07	52.86	77.01	37.74	39.36	96.14	51.59	56.66	93.62	42.33	47.50	91.96	0.39K
β=1.0	82.70	52.86	76.63	38.51	39.70	96.11	52.08	56.79	93.72	41.99	47.52	91.93	0.40K
Effect of ϵ_{sat} (saturation suppression threshold).													
ϵ_{sat}=1e^{-3}	82.87	51.53	76.78	37.09	38.29	96.00	52.14	56.72	93.66	42.20	47.22	91.97	0.45K
ϵ_{sat}=5e^{-3}	83.07	52.86	77.01	37.74	39.36	96.14	51.59	56.66	93.62	42.33	47.50	91.96	0.39K
ϵ_{sat}=1e^{-2}	82.83	53.27	76.40	37.67	39.10	96.20	51.27	56.11	93.65	41.78	47.08	91.91	0.61K
Robustness under noisy threshold perturbation.													
W/o Noise	83.07	52.86	77.01	37.74	39.36	96.14	51.59	56.66	93.62	42.33	47.50	91.96	—
$[-10\%, +10\%]$	82.87	52.33	76.59	37.63	39.05	96.13	51.43	56.72	93.61	42.15	47.38	91.93	—
Cross-model scaling: Photon with different backbone and sizes.													
Photon (Q2.5VL 3B)	83.07	52.86	77.01	37.74	39.36	96.14	51.59	56.66	93.62	42.33	47.50	91.96	0.39K
Photon (Q2.5VL 7B)	83.50	53.90	78.03	40.70	41.90	96.20	53.34	57.65	93.77	42.66	48.14	91.99	0.41K
Photon (Q3VL 2B)	82.28	52.21	75.03	37.65	39.22	95.84	50.59	55.30	93.40	41.30	46.98	91.84	0.37K

Table 9: Token retention and performance on MedFrameQA and SLAKE (accuracy).

Method	MedFrameQA							SLAKE		
	Avg. keep rate.	CT	MRI	X-ray	Other	Ultrasound	Avg. Acc.	Avg. keep	Acc.	Match / Total
Qwen2.5VL 3B	1.000	0.744	0.745	0.893	0.667	0.486	0.727	1.000	0.8446	413/489
Ours 3B	0.432	0.761	0.787	0.857	0.750	0.486	0.745	0.375	0.8425	412/489

accuracy almost unchanged, with only one fewer correct case out of 489. This indicates that the pruning strategy is not tied to CT-specific characteristics and can be applied to other medical imaging modalities.

Extension to video reasoning. Photon can also be applied to video reasoning tasks. In this setting, the base Qwen2.5-VL model is already pre-trained on large-scale visual data, so we simplify the training schedule: the two warmup stages and robustness regularization used for 3D medical training are removed, and the pruning module is trained directly with the main task loss.

To demonstrate this, we apply Photon to the NExT-QA (Xiao et al., 2021) dataset and compare it with the non-pruned Qwen2.5-VL 3B baseline. Table 10 shows that Photon reduces the average token keep rate by more than half while keeping the overall accuracy essentially unchanged. Across causal, descriptive, and temporal question types, the differences remain small, and several categories show slight improvements. This confirms that ITS and SGP can be used in video understanding settings with minimal modifications, providing substantial token reduction without sacrificing performance.

Across CT, MRI, multimodal medical frames, and videos, Photon consistently cuts visual tokens by more than half while keeping accuracy comparable to non-pruned baselines. This shows that the instruction-conditioned pruning design is not restricted to a single imaging protocol or task format and can generalize across diverse modalities and benchmarks.

A.3.1 More visualization results and failure cases.

Qualitative behavior and typical failures. Fig. 7 presents additional visualization results, including both correct predictions and failure cases. Photon successfully identifies major findings such as air bronchogram signs and kidney tumors, but limitations appear in more subtle scenarios. For example, when estimating the size of a nodule on the minor fissure, the model underestimates the measurement (4×3 mm vs. ground-truth 5×3 mm), which reflects the difficulty of precise quantitative reasoning

Table 10: Token retention and performance on NExT-QA (accuracy).

Method	Avg. keep rate	Question type accuracy								Avg. Acc
		Causal-How	Causal-Why	Desc.-Count	Desc.-Loc	Desc.-Other	Temp.-Now	Temp.-Next	Temp.-Present	
Qwen2.5VL 3B	1.000	0.7545	0.7738	0.6429	0.9358	0.8533	0.7760	0.7269	0.7097	0.7729
Ours 3B	0.473	0.7502	0.7693	0.6522	0.9358	0.8483	0.7631	0.7455	0.7527	0.7723

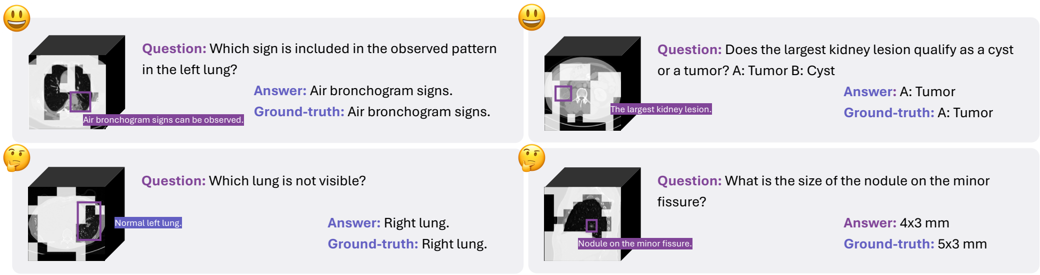
Air bronchogram signs can be observed.
The largest kidney lesion.
Normal left lung.
Nodule on the minor fissure.

Question: Which sign is included in the observed pattern in the left lung?
Answer: Air bronchogram signs.
Ground-truth: Air bronchogram signs.

Question: Does the largest kidney lesion qualify as a cyst or a tumor? A: Tumor B: Cyst
Answer: A: Tumor
Ground-truth: A: Tumor

Question: Which lung is not visible?
Answer: Right lung.
Ground-truth: Right lung.

Question: What is the size of the nodule on the minor fissure?
Answer: 4x3 mm
Ground-truth: 5x3 mm

Figure 7: More visualization results and failure cases by Photon.

on small targets. In the lung visibility case, although the prediction is correct, the pruning behavior removes the invisible lung and retains the normal one. This likely arises because cases with invisible lung fields are rare in the training data, so the model tends to assign higher importance to common anatomical regions. These examples indicate that errors mostly occur in fine-grained quantitative estimation and rare structural patterns.

Type I: small lesion measurements. The first type of failure concerns small lesion measurements, which are inherently more challenging than tasks such as existence detection. The difficulty comes from several factors: the number of annotated cases for tiny lesions is limited, annotations are not fully standardized and show inter-rater variability, and continuous quantities must be expressed using discrete words. As a result, all methods perform worse on measurement than on existence detection. However, Photon still outperforms or is at least comparable to non-pruned baselines on measurement, which suggests that these errors are mainly due to task and supervision limitations rather than instability introduced by token pruning.

Type II: rare or anatomically unusual cases. The second type of failure appears in rare or anatomically unusual cases, where long-tail samples in training make the model rely more strongly on common structures and become more uncertain in rare regions. For example, in the 3D-RAD (Gai et al., 2025) existence detection task, compared with more than one hundred thousand cases in total, some findings only have a few hundred positive case. Such imbalance makes it harder for the model to assign high saliency to uncommon structures, so both attention and pruning can be less reliable in these regions, even when the backbone itself remains stable.

A.3.2 Statistical Analysis on Token Pruning

Task-conditioned token retention. To address whether token dropping depends on instructions, we analyze how task types change retention for the same organ. For lung-related instructions in 3D-RAD, Table 11 reports the average number of retained lung tokens for Image Observation, Anomaly Detection, Medical Measurement, and Existence Detection. Medical Measurement keeps the most tokens, while Existence Detection keeps the fewest. This pattern shows that the retention ratio is not a fixed global rate, but is systematically adjusted according to task type, which supports that pruning is conditioned on the instruction and task semantics.

Spatial dissimilarity across instructions. We further study how the spatial distribution of retained regions changes with different organ-related instructions. We measure Jaccard dissimilarity (defined as 1 minus the overlap) between retained-region masks obtained under different prompts. The right part of Table 11 gives dissimilarity values between organ pairs, which fall in the range 0.52–0.69. These values indicate noticeable but structured changes in the retained regions when the organ in the instruction changes, again suggesting that Photon's pruning responds to semantic differences instead of acting as a fixed spatial mask.

Table 11: Task-conditioned lung token retention (left) and organ-wise Jaccard dissimilarity (right).

Task	Image observation	Anomaly detection	Pair	kidney vs liver	liver vs spleen	kidney vs lung
Avg. retained tokens	485.3	479.6	Dissimilarity	0.6810	0.6646	0.5530
Task	Medical measurement	Existence detection	Pair	liver vs lung	lung vs spleen	kidney vs spleen
Avg. retained tokens	499.5	455.9	Dissimilarity	0.6852	0.5237	0.5247

Table 12: Block-level lung coverage for Photon (3B) on lung-related instructions in 3D-RAD.

Method	Global coverage	Mean per volume coverage
Ours 3B	0.831	0.818

Overlap with lung segmentations. To check whether instruction-conditioned pruning still preserves key anatomical regions, we extract all lung-related instructions from 3D-RAD and perform a block-level overlap analysis between retained tokens and reference lung segmentations on 3D volumes. Pre-trained segmentation models provide the reference lung masks, which are resampled to the token grid used by the pruning module. For each volume, we compute the fraction of lung-positive blocks that are retained and then aggregate these statistics across the lung subset. As shown in Table 12, Photon retains a large fraction of lung parenchyma blocks with consistent coverage across volumes. Given that some lesion-specific queries do not require observing the entire lung parenchyma, this degree of coverage is reasonable. Overall, these visualization and quantitative analyses indicate that Photon's token scheduling is instruction-conditioned: both the number and spatial distribution of retained tokens adapt to the task and target organ.

A.4 Limitations and Future Works

Although our method demonstrates robust empirical performance, prospective clinical validation and human-centric user studies with medical practitioners remain vital for future work. A promising avenue for research involves integrating temporal and longitudinal imaging to facilitate the coherent modeling of disease progression (Wang et al., 2025b;a). Future studies could also investigate the incorporation of reinforcement learning (Jiang et al., 2026; Chen et al., 2025a; Lin et al., 2025c;b) or self-supervised objectives to enable more adaptive token utilization. Furthermore, enhancing computational efficiency through refined KV-Cache management (Wang et al., 2026b) and more inference techniques (Ma et al., 2025) represents a critical direction for further exploration.

Beyond VQA tasks, Photon's utility could be extended to a broader spectrum of clinical applications, including cross-institutional generalization, interactive diagnostic support (Zhang et al., 2025b), and integration into large-scale multimodal pretraining pipelines (Liu et al., 2025a) to accommodate diverse modalities (Fang et al., 2025; Li et al., 2023c; 2025b; Fang et al., 2024). Integrating auxiliary diffusion modules Wang et al. (2026a); Chen et al. (2025b) presents a compelling opportunity to generate more intuitive and interpretable visual results. Combining more tasks like segmentation He et al. (2025); Liu et al. (2025c;d); Wang et al. (2025c; 2024a) is also worth exploring.

A.5 Ethics Statement

This study was conducted in accordance with ethical standards for medical data usage. We obtained authorization to use the DeepTumorVQA (Chen et al., 2025c) and AbdomenAtlas 3.0 datasets (Li et al., 2024a). For the 3D-RAD (Gai et al., 2025) dataset, which is derived from CT-RATE (Hamamci et al., 2024b), we followed the CC BY-NC-SA license under which it is released. All datasets used in this work, whether publicly available or private, were fully de-identified to protect patient privacy. For data requiring explicit authorization, formal permission was obtained for use.

A.6 Reproducibility Statement

To support reproducibility, we provide detailed descriptions of the model architecture, training objectives, training procedures, and optimization settings in the main text and appendix. Experimental configurations, including hyperparameters, evaluation metrics, and implementation details, are documented to enable replication. The relevant source code and evaluation agreements will be released to the community after undergoing institutional review and authorization.

A.7 The Statements of Using Large Language Models

In the preparation of this manuscript, large language models were employed for language polishing and grammar correction. All scientific content, data analyses, results, and conclusions were conceived, conducted, and verified by the authors. The use of LLMs was limited to improving readability and ensuring grammatical accuracy, without generating or altering any substantive scientific material.

B Acknowledgement

This work was supported by the STI 2030-Major Projects under Grant 2021ZD0201404 and Shenzhen Key Laboratory of New Generation Interactive Media Technology Innovation (ZDSYS20210623092001004). This work was also supported by Alibaba Group through Alibaba Research Intern Program.